Biophysical Journal
Article

Biophysical Society

Balance between Force Generation and Relaxation Leads to Pulsed Contraction of Actomyosin Networks

Qilin Yu,[1] Jing Li,[1] Michael P. Murrell,[2,3] and Taeyoon Kim[1,*]
[1]Weldon School of Biomedical Engineering, Purdue University, West Lafayette, Indiana; [2]Department of Biomedical Engineering, Yale University, New Haven, Connecticut; and [3]Systems Biology Institute, Yale University, West Haven, Connecticut

ABSTRACT Actomyosin contractility regulates various biological processes, including cell migration and cytokinesis. The cell cortex underlying the membrane of eukaryote cells exhibits dynamic contractile behaviors facilitated by actomyosin contractility. Interestingly, the cell cortex shows reversible aggregation of actin and myosin called "pulsed contraction" in diverse cellular phenomena, such as embryogenesis and tissue morphogenesis. Although contractile behaviors of actomyosin machinery have been studied extensively in several in vitro experiments and computational studies, none of them successfully reproduced the pulsed contraction observed in vivo. Recent experiments have suggested the pulsed contraction is dependent upon the spatiotemporal expression of a small GTPase protein called RhoA. This only indicates the significance of biochemical signaling pathways during the pulsed contraction. In this study, we reproduced the pulsed contraction with only the mechanical and dynamic behaviors of cytoskeletal elements. First, we observed that small pulsed clusters or clusters with fluctuating sizes may appear when there is subtle balance between force generation from motors and force relaxation induced by actin turnover. However, the size and duration of these clusters differ from those of clusters observed during the cellular phenomena. We found that clusters with physiologically relevant size and duration can appear only with both actin turnover and angle-dependent F-actin severing resulting from buckling induced by motor activities. We showed how parameters governing F-actin severing events regulate the size and duration of pulsed clusters. Our study sheds light on the underestimated significance of F-actin severing for the pulsed contraction observed in physiological processes.

INTRODUCTION

Living cells need to generate mechanical forces for their physiological functions (1). Forces are generated mainly by interactions between actin filaments (F-actin) and myosin II motor proteins in the cell cortex, which is a thin layer beneath the cell membrane (2). Myosin II proteins walk on F-actin by consuming chemical energy stored in ATP, which results in generation of tensile forces. Forces produced from actomyosin contractility facilitate a wide variety of morphogenetic phenomena at cell and tissue scales (3). For example, contractility induces cortical flows of the cortex for formation of cytokinetic furrow and drives polarization in the one-cell-stage *Caenorhabditis elegans* embryo (4,5). In addition, during invagination of *Drosophila* mesoderm cells, anisotropic generation of forces from actomyosin cortex drives apical constriction (6). Interestingly, in these morphogenetic events, the actomyosin cortex exhibits pulsed contraction; F-actin and myosin II proteins show transient accumulation followed by scattering at various length scales rather than irreversible accumulation (5,7). It has been suggested that the local accumulation of F-actin and myosin originates from contractile instability, which inevitably exists in the highly contractile actomyosin cortex (8,9). The contractile instability is controlled by a spatiotemporal oscillator of RhoA that regulates myosin motor activity, which enables cells to use an intrinsically unstable contractile cortex for driving morphogenetic processes. As a result of the instability control, pulsed contraction emerges in the cortex. To understand how actomyosin contractility facilitates these morphogenetic phenomena, various methods have been applied for perturbing the constituents of actomyosin machinery in cells. However, there are limitations on the extent of perturbation, and results obtained

Submitted April 9, 2018, and accepted for publication October 5, 2018.
*Correspondence: kimty@purdue.edu
Qilin Yu and Jing Li contributed equally to this work.
Editor: Vivek Shenoy.
https://doi.org/10.1016/j.bpj.2018.10.008

from perturbation are often too unclear to understand how the actomyosin contractility works in cells.

Thus, alternatively, contractile behaviors driven by the actomyosin contractility have been extensively studied in recent works using computational and theoretical models as well as reconstituted actomyosin systems. It was demonstrated that the architecture and connectivity of actomyosin networks can significantly affect pattern formation (8,10,11). In addition, it was shown that force-dependent unbinding of actin cross-linking proteins (ACPs) from F-actin plays a critical role for a change in force generation and morphology of actomyosin networks (12,13). Recently, buckling of F-actin was found to be crucial for large contraction of networks into small clusters (10,14), consistent with a theoretical prediction (15). We recently suggested that buckling-induced severing of F-actin can also be very important for contraction of actomyosin networks (16). Several recent studies demonstrated that actin turnover stabilizes stress generated by actomyosin networks and helps maintain homogeneous network morphology by counteracting motor activity (17–19). Although these previous studies have provided insights into understanding of contractile behaviors of actomyosin networks in general, most of them could not recapitulate the pulsed contraction observed during morphogenetic events. They showed only existence of two different states: irreversible aggregation without disassembly of clusters after formation or negligible contraction, which represents a homogeneous network. One study showed coalescence and breakage of actomyosin clusters observed in their in vitro experiments. However, it used an artificial assumption for the phenomenological model that the unbinding rate of motors highly increases within clusters to enforce clusters to spontaneously break into two or three pieces. In addition, their observation on the coalescence and breakage of clusters is intrinsically different from the pulsed contraction that occurs via gradual growth and shrinkage of clusters. A recent computational study claimed that pulsed contraction can appear when F-actins turn over (20). However, they simulated the actin turnover by removing and adding entire F-actins at a fixed rate, which may not be physiologically relevant. In addition, the size of clusters emerging in their simulation showed fluctuation without complete disassembly of clusters. The lack of observations on the pulsed contraction in these previous computational, theoretical, and in vitro studies raises the question of whether the spatiotemporal biochemical control is indispensable for pulsed contraction of actomyosin networks.

To address this question and identify the necessary conditions for the emergence of pulsed contraction, we employed a well-established agent-based model for simulating a very thin actomyosin network consisting of F-actin, motor, and ACPs (12,16,17,21). First, we explored parametric spaces consisting of the turnover rate and length of F-actin and the density of ACPs to identify the regimes in which pulsed contraction occurs. Via quantitative analysis of dynamic changes in network morphology, we found the pulsed contraction can appear without the spatiotemporal biochemical control if force generation from motors is in the balance with force relaxation induced by F-actin treadmilling. However, we observed that the average size of clusters formed during pulsed contraction is much smaller than that observed during the morphogenetic events. If cluster size increases beyond a critical level, the clusters either continuously grow or shrink slowly. We found that inclusion of buckling-induced severing of F-actin enables larger clusters to be disassembled quickly, leading to strong pulsed contraction with much larger clusters. However, if there is only severing without treadmilling, F-actins are shortened over time and thus unable to form large pulsed clusters consistently. We concluded that both local force relaxation via F-actin severing and turnover of F-actin via treadmilling are necessary for strong pulsed contraction in actomyosin networks.

METHODS

Model overview

For simulations in this study, we employed our well-established agent-based model of actomyosin networks based on Brownian dynamics (12,16,17,21). Basic features and parameters of the model are described in detail in the Supporting Materials and Methods and Table S1. In the model, F-actin, motor, and ACPs are simplified by cylindrical segments (Fig. S1 *a*). F-actin is simplified into serially connected cylindrical segments of 140 nm in length with polarity barbed and pointed ends. Motors are modeled after myosin thick filaments: they have a backbone structure with four arms attached, and each arm represents eight myosin heads. ACPs consist of two cylindrical segments. Displacements of the cylindrical segments at each time step are calculated by the Langevin equation with Euler integration scheme in the absence of inertia. Stochastic force in the Langevin equation determined based on the fluctuation-dissipation theorem leads to thermal fluctuations (22). Deterministic forces include bending and extensional forces that maintain equilibrium angles formed by segments and equilibrium lengths of segments, respectively, as well as repulsive force between neighboring pairs of segments to consider volume-exclusion effects. ACPs bind to F-actin with no preference of cross-linking angle at a constant rate and also unbind from F-actin at a force-dependent rate described by Bell's law (23); an unbinding rate exponentially increases as ACP experiences larger tensile forces. Each arm of motors binds to F-actin at a constant rate and then walks toward the barbed end of F-actin at a force-dependent rate; a walking rate decreases as the arm feels higher tensile force. Thus, the arm stops walking if applied force on each myosin head is larger than the stall force. The motor arm unbinds from F-actin at a rate inversely proportional to applied force. The force-dependent walking and unbinding rates of motor arms are determined by a theoretical model called the parallel cluster model (24,25). For all simulations in this study, we employed a very thin computational domain ($10 \times 10 \times 0.1$ μm) with periodic boundary conditions only in the x and y directions (Fig. S1 *b*). In the z direction, boundaries of the domain exert repulsive forces on elements that are displaced beyond the boundaries. At the beginning of each simulation, a thin actomyosin network is formed via self-assembly of F-actin, ACPs, and motor.

Actin dynamics

Formation of F-actin begins from a nucleation event with appearance of one cylindrical segment with polarity in a random direction perpendicular

to the z direction. Polymerization and depolymerization of actins are simulated by addition and removal of one cylindrical segment, respectively, as in our previous studies (17). Via spatiotemporal control of rate constants governing the nucleation, polymerization, and depolymerization, we can simulate various types of actin turnover facilitated by actin binding proteins, such as cofilin, formin, and capping proteins. However, to avoid unnecessary complexity and uncertainty, we employed the simplest form of actin turnover, treadmilling (17). To mimic the F-actin treadmilling, we assumed that polymerization and depolymerization occur only at barbed ends and pointed ends, respectively. It was further assumed that a rate constant governing polymerization ($k_{+,\mathrm{A}}$) has the same value as that governing depolymerization ($k_{-,\mathrm{A}}$), which results in a dynamic equilibrium at an actin concentration of 1 μM. We define a turnover rate ($k_{\mathrm{t,A}}$) to indicate the rate of actin treadmilling, and the value and unit of $k_{\mathrm{t,A}}$ are identical to those of $k_{-,\mathrm{A}}$. By adjusting the ratio of the nucleation rate constant ($k_{\mathrm{n,A}}$) to $k_{\mathrm{t,A}}$, the average length of F-actin ($<L_{\mathrm{f}}>$) is varied between 0.7 and 5.0 μm. This range of $<L_{\mathrm{f}}>$ is smaller than that used in typical reconstituted actomyosin networks without control of F-actin length ($\sim$20 μm) (26,27). However, the range is very comparable to that estimated in the cell cortex (28,29).

In addition, for some of the simulations, we employed angle-dependent F-actin severing as in our recent work (16). F-actin severing is mimicked in a simulation by eliminating one actin segment on F-actin. To determine a segment to eliminate, the sum of bending angles at two ends of each actin segment ($\theta_{\mathrm{s,A}}$) is calculated. Then, the severing rate ($k_{\mathrm{s,A}}$) is calculated from the sum using the following relationship:

$$k_{\mathrm{s,A}} = k^0_{\mathrm{s,A}} \exp\left(\frac{\theta_{\mathrm{s,A}}}{\lambda_{\mathrm{s,A}}}\right), \tag{1}$$

where $k^0_{\mathrm{s,A}}$ is a zero-angle severing rate constant and $\lambda_{\mathrm{s,A}}$ is insensitivity to $\theta_{\mathrm{s,A}}$. The insensitivity means that as $\lambda_{\mathrm{s,A}}$ is higher, severing events tend to occur at larger bending angles. Because $\theta_{\mathrm{s,A}}$ is the sum of two angles, an increase in a bending angle on either end of an actin segment can lead to disappearance of the segment because of severing. The relationship in Eq. 1 was found empirically by comparing with in vitro experiments (30) as explained and justified in the Supporting Materials and Methods in detail. Although we devised Eq. 1 without a rigorous physical basis, it reflects an experimental observation that severing takes places only at a large bending angle (i.e., a small radius curvature). As explained in the Supporting Materials and Methods, our results are insensitive to the choice of a specific model for F-actin severing.

Analysis of motions of motors

To evaluate how fast motors move at each time point, we quantify their average speed. We track the center position of each motor over time, $\mathbf{r}_{i,\mathrm{M}}$, where i is an index of a motor. Because the domain is very thin in the z direction, we assumed that $\mathbf{r}_{i,\mathrm{M}}$ has only x and y components. Then, ensemble average of speed of motors is calculated every 1 s:

$$\begin{aligned}\langle v_{\mathrm{M}}(t)\rangle &= \frac{1}{N_{\mathrm{M}}}\sum_{i=1}^{N_{\mathrm{M}}} v_{i,\mathrm{M}}(t) \\ &= \frac{1}{N_{\mathrm{M}}}\sum_{i=1}^{N_{\mathrm{M}}} \frac{|\mathbf{r}_{i,\mathrm{M}}(t) - \mathbf{r}_{i,\mathrm{M}}(t-1)|}{1\ \mathrm{s}},\end{aligned} \tag{2}$$

where N_{M} is the total number of motors. For a certain time range, we calculate time average of the ensemble average:

$$\langle v_{\mathrm{M}}\rangle_{t_1\to t_2} = \frac{1}{t_2 - t_1}\sum_{t=t_1}^{t_2}\langle v_{\mathrm{M}}(t)\rangle, \tag{3}$$

where t_1 and t_2 are lower and upper limits of the time range of interest. If the time interval is shorter than 1 s, the calculated speed becomes noisier because influences of thermal fluctuation on motor motions are not averaged out sufficiently. If the time interval is too long, the number of data points is not enough to calculate $\langle v_{\mathrm{M}}\rangle_{t_1\to t_2}$. We therefore used the time interval of 1 s for the best analysis of motor motions.

Evaluation of network morphology

We evaluate the heterogeneity of network morphology by measuring spatial distributions of F-actins in the computational domain. For measurement, the domain is divided into $N_{\mathrm{G}} \times N_{\mathrm{G}}$ grids in the x and y directions, where N_{G} indicates the number of grids in each direction. Each grid has its coordinate, (i, j). We measure the number of actin segments located in each grid, $\rho_{\mathrm{A}}^{i,j}$, to create the three-dimensional histogram representing their density map. Then, SD of $\rho_{\mathrm{A}}^{i,j}$ calculated over all grids is considered as an indicator for the heterogeneity of network morphology, Q_{A}. Because the heterogeneity calculated in this method depends on the choice of N_{G}, we carefully determined the optimal range of $N_{\mathrm{G}} = 10$–20.

As an additional measure for heterogeneity, we employ an analysis method used in a previous study (31). First, we randomly choose 1% of actin segments and calculate distances between them. We calculate a radial distribution function, $g(r)$, as a histogram with a bin size δr:

$$g(r) = P(r)/(2\pi r \delta r \rho_a), \tag{4}$$

where ρ_{a} represents the density of selected actin segments calculated over a whole network and $P(r)$ is the probability of actin segments with a separate distance between r and $r + \delta r$. r is varied from 50 nm to 1 μm with an increment of $\delta r = 50$ nm. Smaller δr enables smoother radial distribution curve and transition. Higher peaks at low r indicate that a network is highly heterogeneous. By contrast, a very homogeneous network leads to $g(r) \sim 1$ for all r values.

Quantification of clustering behaviors

We probed the onset and emergence of pulsed contraction in an actomyosin network. In the density map of actin segments explained above, all adjacent grids whose density and duration are above threshold values are grouped and considered to be a single cluster (Fig. S1 *c*). Because results of quantification can significantly vary depending on the threshold value, we carefully chose the threshold values of density and duration as explained in the Supporting Materials and Methods. Then, we calculated the center position of each cluster and the number of actin segments that belong to each cluster. This analysis was repeated for all data recorded every 1 s. We then correlated clusters at one time point to those at the next time point. Two clusters in consecutive time points were regarded as the same cluster if two primary criteria were met. First, the distance between centers of two clusters could not be larger than a chosen threshold. The threshold value was assumed to be proportional to the size of the clusters. Second, the difference in the number of actin segments in the two clusters could not be larger than half of the number of actin segments in the cluster at a later time point. When two or more clusters were merged, one of the clusters at a previous time point would share the same identity of a merged cluster at the next time point. Only the cluster with the longest history was kept. For instance, if two clusters that were merged later started emerging from different time points, the one that formed earlier would be kept and linked to the merged cluster, whereas the other that formed later would be ignored for the analysis. In addition, we ignored clusters that lasted for less than 20 s to avoid counting trivial small structures. The threshold value for the minimal duration was also chosen carefully as explained in the Supporting Materials and Methods.

Formation of clusters requires persistent movement of motors toward a specific point. We probed how persistently motors move over time. First,

we calculated the ensemble average of velocities of all motors located in each grid, $\mathbf{v}_{\mathrm{M}}^{i,j}(t)$, and then analyzed the autocorrelation of $\mathbf{v}_{\mathrm{M}}^{i,j}$ as a measure for persistency of the velocities over time:

$$\langle \cos\phi(t)\rangle = \frac{1}{N_{\mathrm{G}}^2}\sum_{i=1}^{N_{\mathrm{G}}}\sum_{j=1}^{N_{\mathrm{G}}}\cos\phi_{i,j}(t) = \frac{1}{N_{\mathrm{G}}^2}\sum_{i=1}^{N_{\mathrm{G}}}\sum_{j=1}^{N_{\mathrm{G}}}\frac{\mathbf{v}_{\mathrm{M}}^{i,j}(t)\cdot\mathbf{v}_{\mathrm{M}}^{i,j}(t+\tau)}{\left|\mathbf{v}_{\mathrm{M}}^{i,j}(t)\right|\left|\mathbf{v}_{\mathrm{M}}^{i,j}(t+\tau)\right|}, \quad (5)$$

where τ is 1 s. Values of $\langle\cos\phi\rangle$ are averaged between 10 and 20 s, representing dynamics of the motors at early time points when a network exhibits very active aggregating behaviors in all cases. Note that the average value of $\langle\cos\phi\rangle$ close to 1 is indicative of very persistent motions of motors, which are the signature of clustering.

RESULTS

In this study, we performed simulations under various conditions to study the contractile behaviors of two-dimensional actomyosin networks. We varied the turnover rate ($k_{\mathrm{t,A}}$), severing rate ($k_{\mathrm{s,A}}$), and average length ($<L_{\mathrm{f}}>$) of F-actin and cross-linking density (R_{ACP}) in the simulations, whereas we fixed actin concentration (C_{A}) at 60 μM and motor density (R_{M}) at 0.04.

Turnover of F-actin suppresses formation of clusters

In recent computational studies (18–20,32–34), it was shown that actin turnover prevents motors from forming aggregation in two-dimensional and three-dimensional actomyosin networks as well as stabilizing stress generated from the networks by relaxing forces produced from motor activities. As in our previous study (17), we implemented the simplest form of turnover, treadmilling of F-actin, by imposing identical rate constants for polymerization at a barbed end and depolymerization at a pointed end. Despite its simplicity, the treadmilling is more realistic turnover dynamics than the abrupt disappearance and appearance of F-actins employed in recent computational studies (18–20).

We imposed $k_{\mathrm{t,A}}$, which represents a treadmilling rate, between 15 and 240 s^{-1} with R_{ACP} = 0.02 and $<L_{\mathrm{f}}>$ = 1.6 μm. With the lowest $k_{\mathrm{t,A}}$ = 15 s^{-1}, a large portion of a network aggregates into a large cluster, resulting in very heterogeneous F-actin distribution (Fig. 1, *a* and *b* and S2 *a*). However, as $k_{\mathrm{t,A}}$ increases, networks tend to be more homogeneous with less distinct, smaller clusters as force relaxation is elevated. We also analyzed motor activities in a quantitative manner. With lower $k_{\mathrm{t,A}}$, motors move persistently toward centers of the clusters and move much more slowly after formation of clusters (Fig. 1, *b* and *c*). With higher $k_{\mathrm{t,A}}$, motors exhibit less persistent movements because motors cannot stably walk on F-actins that turn over rapidly via treadmilling (Fig. 1 *b*). In addition, because a network does not aggregate significantly, the average speed of motors does not change much over time (Fig. 1 *c*).

Network connectivity critically affects contraction

It has been shown that network connectivity plays a critical role for contractile behaviors of actomyosin networks (10). We recently demonstrated that a cross-linked actomyosin network in the absence of actin turnover shows maximal contraction at intermediate level of R_{ACP} because poor connectivity prevents motors from stably generating forces between pairs of F-actins, whereas too-high connectivity leads to strong resistance of the network to contraction because of high network elasticity (16). This is consistent with previous

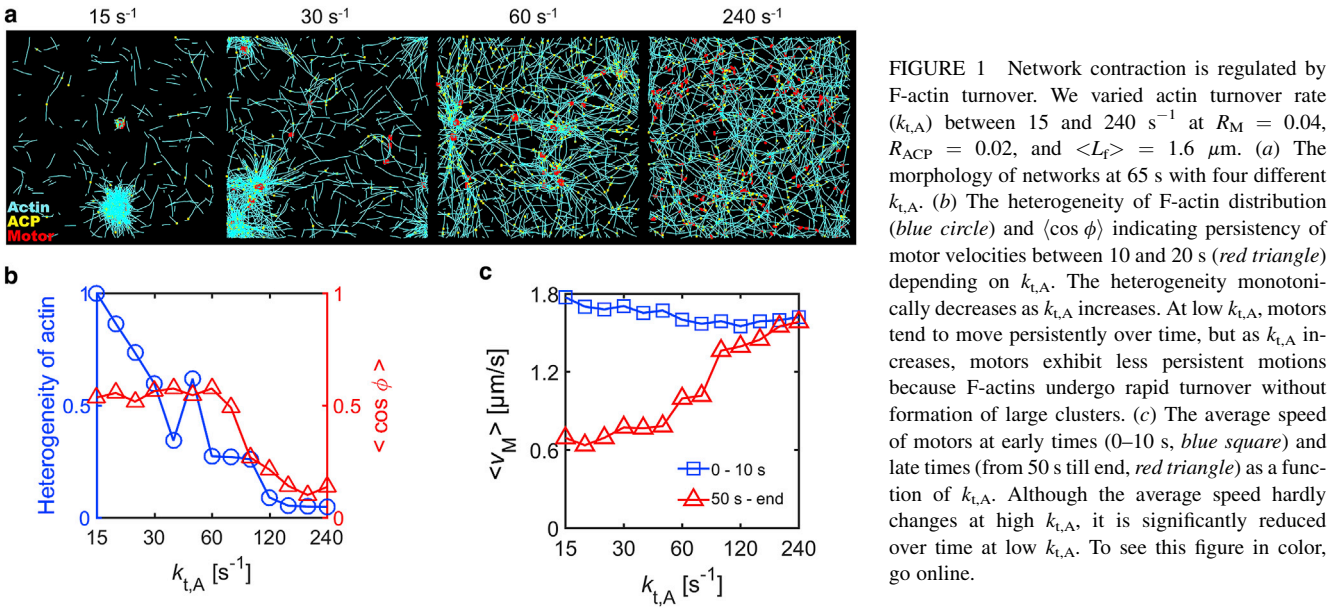

FIGURE 1 Network contraction is regulated by F-actin turnover. We varied actin turnover rate ($k_{\mathrm{t,A}}$) between 15 and 240 s^{-1} at R_{M} = 0.04, R_{ACP} = 0.02, and $<L_{\mathrm{f}}>$ = 1.6 μm. (*a*) The morphology of networks at 65 s with four different $k_{\mathrm{t,A}}$. (*b*) The heterogeneity of F-actin distribution (*blue circle*) and $\langle\cos\phi\rangle$ indicating persistency of motor velocities between 10 and 20 s (*red triangle*) depending on $k_{\mathrm{t,A}}$. The heterogeneity monotonically decreases as $k_{\mathrm{t,A}}$ increases. At low $k_{\mathrm{t,A}}$, motors tend to move persistently over time, but as $k_{\mathrm{t,A}}$ increases, motors exhibit less persistent motions because F-actins undergo rapid turnover without formation of large clusters. (*c*) The average speed of motors at early times (0–10 s, *blue square*) and late times (from 50 s till end, *red triangle*) as a function of $k_{\mathrm{t,A}}$. Although the average speed hardly changes at high $k_{\mathrm{t,A}}$, it is significantly reduced over time at low $k_{\mathrm{t,A}}$. To see this figure in color, go online.

experimental results (35) and reproduced in another computational study later (20).

In the presence of slow actin turnover ($k_{t,A} = 30\ s^{-1}$), we systematically tested influences of R_{ACP} and $<L_f>$ that are likely to govern network connectivity. It was observed that a change in R_{ACP} and $<L_f>$ has similar effects on network contraction. With very poor network connectivity due to low R_{ACP} or $<L_f>$, a network hardly contracts or contracts into multiple small clusters, but as connectivity increases, a single, large cluster is formed from aggregation of F-actins (Figs. 2 *a* and 3 *a*). A further increase in connectivity suppresses formation of disconnected clusters, resulting in a network consisting of interconnected bundles. Thus, at intermediate connectivity, spatial distribution of F-actins is the most heterogeneous, and motors exhibit the most persistent movements toward centers of large clusters (Figs. 2 *b*, 3 *b*, and S2, *b* and *c*). In addition, the average speed of motors at early times is the highest at intermediate connectivity because of large contraction into a single cluster (Figs. 2 *c* and 3 *c*). The average speed becomes much lower at late times in most cases in which networks show large contraction into clusters or bundle networks. However, at very low R_{ACP}, a decrease in the average speed of motors is less significant because the network does not form distinct clusters.

Weak pulsed contraction appears to be due to balance between force generation and relaxation

By analyzing morphological changes in networks, we probed the existence of pulsed contraction. Under specific conditions, we observed weak pulsed contraction with very small clusters. F-actins and motors aggregate toward a focal point, but nascent small clusters are disassembled shortly after formation without an increase in their size (Fig. 4, *a* and *b*), indicating pulsed contraction. This weak pulsed contraction originates from subtle balance between force generation from motor activities and force relaxation induced by actin turnover. To identify types of clusters based on size and duration, we traced individual clusters and measured the percentage of actin segments that belong to each cluster over time. These small pulsed clusters appear by themselves at higher $k_{t,A}$ (Fig. S3 *a*; Video S1). However, at lower $k_{t,A}$, they appear with some small clusters that fluctuate in their size till the end of simulations (Fig. 4, *a*, *c*, and *d*; Video S2). An apparent difference between the nascent pulsed clusters and fluctuating clusters is whether or not complete disassembly occurs soon after formation. Fluctuating clusters form because force relaxation is not fast enough to relax forces generated by actomyosin components. We evaluated the size and duration of nascent clusters during the weak pulsed contraction (Fig. 4, *e* and *f*). The clusters are quite small and do not last for a long time, with lifetimes shorter than 50 s. Note that pulsed clusters observed in cells are typically ~2–4 μm in diameter and ~40–100 s in duration (36).

A previous computational study that demonstrated pulsed contraction with larger clusters employed a different way to account for actin turnover (20). In their model, a whole F-actin is randomly removed in a domain, and a new F-actin appears in a different location as in other studies (18). Such turnover of entire F-actins can break down multiple connections in clusters at once, enabling large clusters to be disassembled. Although this is an efficient way to induce local, strong force relaxation for pulsed contraction, it is much less physiological than our turnover model. Indeed, pulsed contraction observed in the recent study is more similar to the behavior of

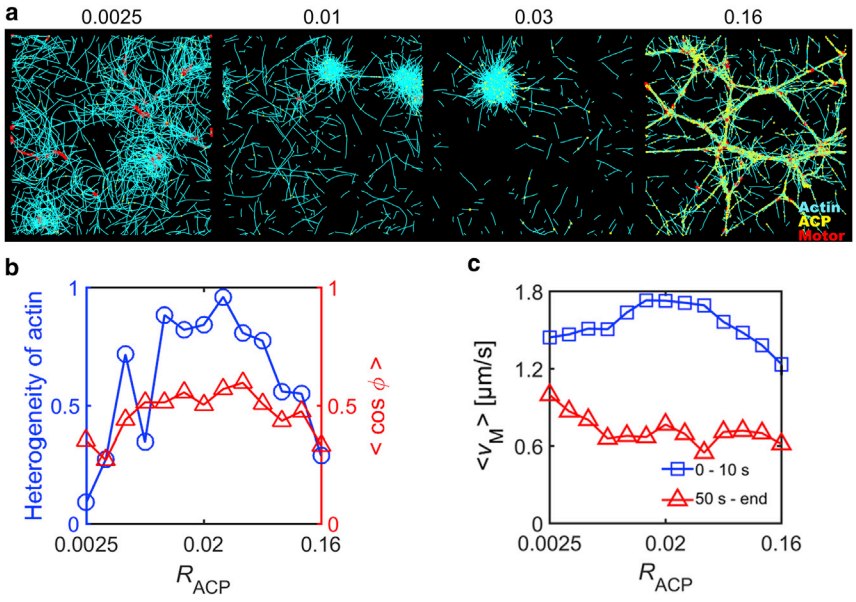

FIGURE 2 Actin cross-linking proteins (ACPs) regulate contractile behaviors of networks. We changed ACP density (R_{ACP}) between 0.0025 and 0.16 at $R_M = 0.04$, $<L_f> = 1.6\ \mu$m, and $k_{t,A} = 30\ s^{-1}$. (*a*) The morphology of networks at 65 s depending on R_{ACP}. At small R_{ACP}, networks are quite homogeneous. As R_{ACP} increases, networks severely aggregate into disconnected clusters. At large R_{ACP}, very high network connectivity precludes formation of separated clusters, leading to interconnected bundles. (*b*) The heterogeneity of F-actin distribution (*blue circle*) and $\langle \cos \phi \rangle$ representing persistency of motor velocities between 10 and 20 s (*red triangle*) depending on R_{ACP}. Consistent with (*a*), the heterogeneity is the highest at intermediate levels of R_{ACP}, and velocities of motors exhibit the most persistent motions. (*c*) The average speed of motors at early times (0–10 s, *blue square*) and late times (from 50 s till end, *red triangle*). Motors initially move at the highest speed at intermediate levels of R_{ACP} at which the largest contraction emerges. Regardless of R_{ACP}, the average speed is substantially decreased over time. To see this figure in color, go online.

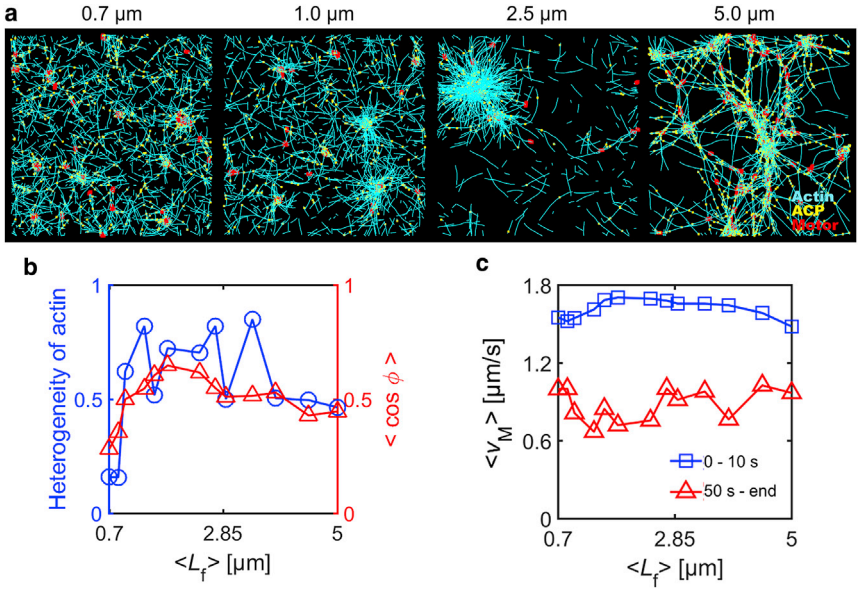

FIGURE 3 Average length of F-actins ($<L_f>$) highly affects network contraction in a similar fashion to R_{ACP}. We varied $<L_f>$ between 0.7 and 5.0 μm at $R_M = 0.04$, $R_{ACP} = 0.02$, and $k_{t,A} = 30\ s^{-1}$. (*a*) The morphology of networks at 56 s with different $<L_f>$. With short F-actins, only small clusters appear, whereas larger clusters are formed with longer F-actins. If F-actins are very long, enhanced network connectivity precludes formation of separated clusters, leading to interconnected bundles. (*b*) The heterogeneity of F-actin distribution (*blue circle*) and $\langle \cos \phi \rangle$ indicative of persistency of motor velocities between 10 and 20 s (*red triangle*) depending on $<L_f>$. The heterogeneity and persistency are the largest at intermediate levels of $<L_f>$ because of the largest contraction. (*c*) The average speed of motors at early times (0–10 s, *blue square*) and late times (from 50 s till end, *red triangle*) as a function of $<L_f>$. Initial average speed is the highest at intermediate levels of $<L_f>$ because of the largest contraction. At all values of $<L_f>$, the average speed is decreased significantly over time. To see this figure in color, go online.

fluctuating clusters in our study because sizes of their clusters showed consistent fluctuation without complete disassembly (20).

If we lower $k_{t,A}$ further, most of the clusters either grow consistently for longer than 100 s until the end of simulation or show relatively fast growth followed by very slow decay,

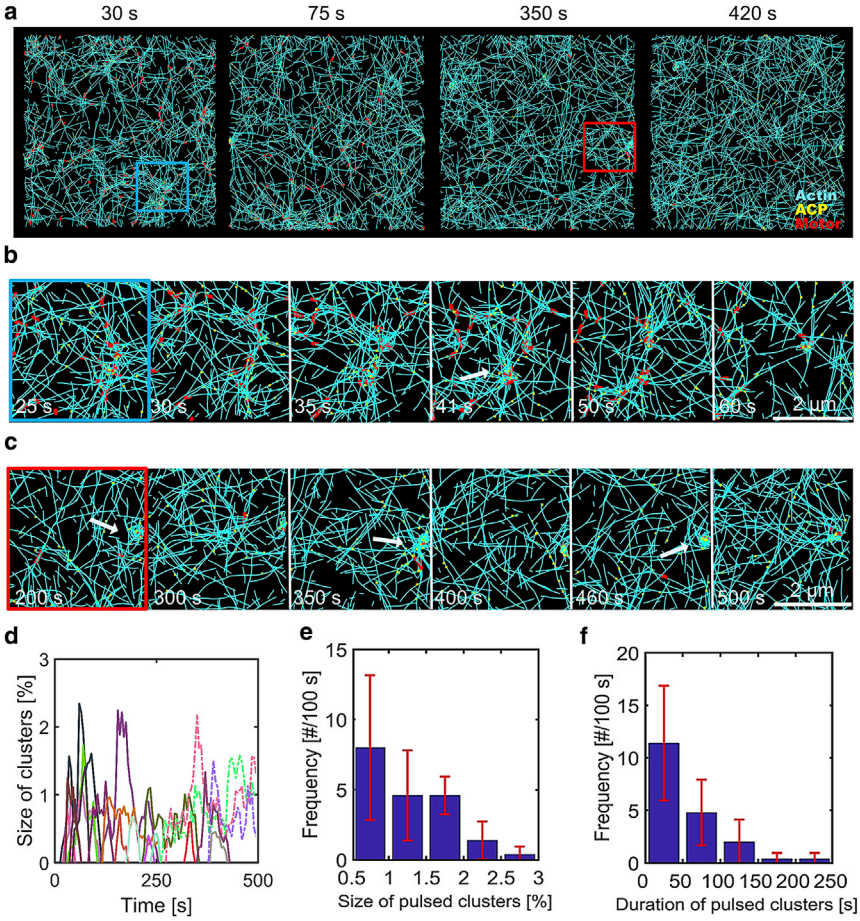

FIGURE 4 Balance between force generation and relaxation causes weak pulsatile contraction with formation of very small clusters. Conditions used in a case shown here are $R_M = 0.04$, $R_{ACP} = 0.01$, $<L_f> = 1\ \mu$m, and $k_{t,A} = 70\ s^{-1}$. (*a*) The morphology of networks showing cluster formation taken at different time points. (*b*) The time evolution of a small pulsed cluster indicated by a blue box in (*a*). This cluster appears from ~30 s and then becomes the largest at 41 s, as indicated by a white arrow. Then, it disassembles gradually over time. (*c*) The time evolution of a fluctuating cluster highlighted by a red box in (*a*). (*d*) The time evolution of the percentage of actin segments located within clusters. Random colors are assigned to curves to distinguish each cluster. Nascent pulsed clusters are shown in solid lines, whereas fluctuating clusters are shown in dot-dashed lines. (*e* and *f*) The frequency of appearance of pulsed clusters per 100 s depending on their size (*e*) and duration (*f*). Most clusters are very small and do not last for long time periods. To see this figure in color, go online.

although some small nascent clusters still form at early times (Fig. S3 *b*; Video S3). None of these clusters are analogous to the pulsed clusters observed in cells in terms of size and duration (36). Thus, it is expected that an additional mechanism of force relaxation is necessary for enabling larger clusters to be disassembled completely within a reasonable time range. Note that in all of these simulations, the average length of F-actins remains relatively constant ($\sim$1 μm) over time and is independent of $k_{t,A}$ (Fig. S3 *c*).

In addition, we quantified cluster dynamics in a wide parametric space consisting of $<L_f>$, $k_{t,A}$, and R_{ACP} (Fig. S3, *d* and *e*). It was observed that the small nascent pulsed clusters appear only in a very narrow regime with short $<L_f>$ ($\sim$1 μm), intermediate actin turnover rate ($\sim$70 s^{-1}), and low/intermediate network connectivity. It is likely that most of the previous computational studies investigating contractile behaviors of actomyosin networks neglected the appearance of the nascent pulsed clusters because they appear in such a narrow regime.

Angle-dependent severing of F-actin facilitates strong pulsed contraction

A recent in vitro experiment clearly demonstrated that F-actins undergo severe fragmentation during contraction of actomyosin networks (14). This fragmentation is likely to originate from angle-dependent severing of F-actin induced by buckling. Our recent computational study also showed that frequent severing events of F-actin can inhibit network contraction (16). Because F-actin is prone to buckling and more severing at the location where contraction takes place, the severing may relax forces locally within contracting clusters and thus help disassembly of larger clusters for more distinct pulsed contraction. We employed the model of angle-dependent F-actin severing used in our previous study to check influences of severing on the pulsed contraction (16). We incorporated F-actin severing in a case that showed formation of relatively large clusters without pulsed contraction and varied the zero-angle severing rate constant ($k^0_{s,A}$) between 10^{-60} and 10^{-10} s^{-1}. It was observed that average length of F-actins remains close to an initial value ($\sim$1 μm) in all simulations except a case with $k^0_{s,A} = 10^{-10}$ s^{-1} (Fig. S4 *g*). When $k^0_{s,A}$ is very low ($=10^{-60}$ s^{-1}), severing events hardly occur, so large irreversible clusters are formed (Fig. S4 *a*). With intermediate values of $k^0_{s,A}$ (10^{-50}–10^{-30} s^{-1}), large clusters are still formed, but many of them are disassembled much faster than decaying clusters, indicative of strong pulsed contraction (Figs. 5, *a* and *b* and S4, *b–d*). The size and duration of these clusters are very comparable to those of pulsed clusters observed in vivo. It was found that more than half of the severing events take place within clusters at these $k^0_{s,A}$ values (Fig. 5 *c*), which implies that buckling arising from contraction of clusters induces F-actin severing and thus relaxation of forces generated by motors within clusters. Note that at 10^{-50} $s^{-1} \leq k^0_{s,A} \leq 10^{-20}$ s^{-1}, a greater number of smaller clusters with shorter lifetime (<50 s) emerged with higher $k^0_{s,A}$ (Fig. 5, *c–e*). In addition, the percentage of severing events occurring within clusters decreases, meaning that severing takes place in a less selective manner. If $k^0_{s,A}$ increases more to 10^{-10} s^{-1}, only a few small pulsed clusters are formed (Fig. 5, *a* and *c–e*). If $k^0_{s,A}$

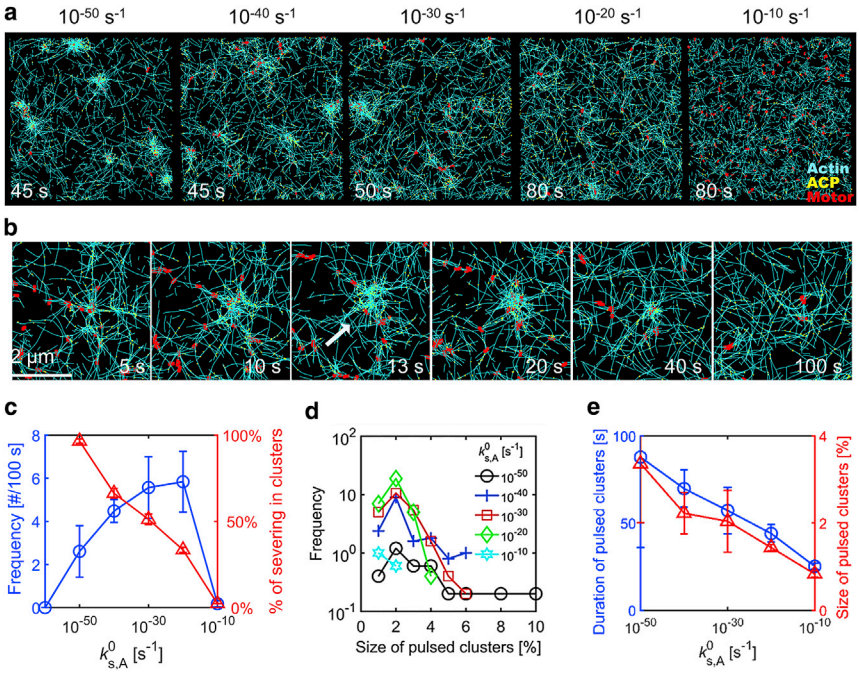

FIGURE 5 Severing of F-actin facilitates strong pulsed contraction via selective force relaxation within clusters. We varied the zero-angle severing rate constant ($k^0_{s,A}$) between 10^{-60} and 10^{-10} s^{-1} at $R_M = 0.04$, $R_{ACP} = 0.02$, $<L_f> = 1$ μm, $k_{t,A} = 30$ s^{-1}, and $\lambda_{s,A} = 1.6°$. (*a*) The morphology of networks with various $k^0_{s,A}$. As $k^0_{s,A}$ increases, clusters become apparently smaller. (*b*) The time evolution of a relatively large pulsed cluster. The cluster appears at $\sim$5 s and becomes the largest at 13 s, as marked by a white arrow. Then, it disassembles completely at $\sim$100 s. (*c*) The frequency of appearance of pulsed clusters per 100 s (*blue circle*) and percentage of severing events occurring within pulsed clusters (*red triangle*) depending on $k^0_{s,A}$. As $k^0_{s,A}$ increases, more pulsed clusters appear, and more severing events take place outside the pulsed clusters. However, few pulsed clusters are formed if $k^0_{s,A}$ is too high. (*d*) The distribution of size of pulsed clusters depending on $k^0_{s,A}$. With lower $k^0_{s,A}$, larger pulsed clusters are more likely to emerge. (*e*) Average duration (*blue circle*) and size (*red triangle*) of the largest pulsed clusters found from each of five simulations with different $k^0_{s,A}$. With lower $k^0_{s,A}$, more larger clusters appear and last longer before complete disassembly. To see this figure in color, go online.

is very high, network connectivity is deteriorated, so contraction is impeded.

We also tested the effects of the insensitivity of F-actin severing to a bending angle ($\lambda_{s,A}$). As explained in the Methods, with higher $\lambda_{s,A}$, severing occurs at larger bending angles. At the range of $\lambda_{s,A}$ tested in this study, the average length of F-actins does not show strong dependence on $\lambda_{s,A}$ (Fig. S5 *h*). The total number of pulsed clusters is not affected much by $\lambda_{s,A}$ (Fig. 6 *b*), but more large clusters appear with higher $\lambda_{s,A}$ (Figs. 6 *c* and S5, *a–g*; Video S4). The size and duration of the largest cluster in each simulation are proportional to $\lambda_{s,A}$ (Fig. 6 *d*). If severing is very sensitive to bending angles because of small $\lambda_{s,A}$, a large portion of F-actins within clusters are severed before substantial growth of the clusters, resulting in small pulsed clusters with short lifetime. By contrast, with large $\lambda_{s,A}$, the severing is delayed till F-actins are subject to greater bending angles within larger clusters, leading to formation of large pulsed clusters with relatively long lifetime. In addition, the F-actin severing is more likely to occur within clusters if $\lambda_{s,A}$ is higher (Fig. 6 *b*).

As shown above, both an increase in $\lambda_{s,A}$ and a decrease in $k^0_{s,A}$ lead to formation of more large pulsed clusters. However, their impacts on small pulsed clusters are quite different. Because an increase in $\lambda_{s,A}$ hardly affects the frequency of emergence of small pulsed clusters (Fig. 6 *c*), large pulsed clusters coexist with small ones at high $\lambda_{s,A}$ (Fig. 6 *a*). By contrast, a decrease in $k^0_{s,A}$ drastically reduces emergence of small pulsed clusters (Fig. 5 *d*), so large pulsed clusters appear without many small pulsed clusters (Fig. 5 *a*). Thus, to finely tune populations of small and large pulsed clusters, regulation of both $k^0_{s,A}$ and $\lambda_{s,A}$ is necessary.

All of these results imply that in addition to F-actin turnover (i.e., treadmilling), severing results in local force relaxation that helps disassembly of otherwise irreversible large clusters. However, with only severing, strong pulsed contraction cannot last for long time because F-actins are gradually fragmented into shorter filaments over time (Figs. S6 and S7; Video S5). Actin turnover based on treadmilling helps remove the shorter filaments and recycle actin monomers to form another F-actin in a different location, resulting in a relatively constant average length of F-actins over time. Thus, with the presence of both actin treadmilling and severing, the strong pulsed contraction with large clusters with long lifetime can appear.

DISCUSSION

The actomyosin cortex facilitates various morphogenetic events by spatiotemporally regulating its cortical tension. The cortex usually shows homogeneous morphology and bears tensile forces. In our previous studies (12,17), we showed that an actomyosin network cross-linked by transient ACPs can maintain homogeneous morphology and generate sustainable tensile forces in two ways. If there is no F-actin turnover, the number of active motors generating forces should be small enough to result in only a small load on each ACP. If F-actin undergoes relatively fast turnover, a network with a large number of active motors can be stable because the F-actin turnover prevents motors from developing large forces. Based on observations in previous experiments (10,17,37–39), it is likely that the actomyosin cortex in cells can be stable because of F-actin turnover. For example, when F-actin turnover was perturbed by drugs, the actomyosin cortex formed aggregates and lost most of its traction forces.

In recent experiments (7,40,41), it has been observed that the actomyosin cortex exhibits pulsed contraction during

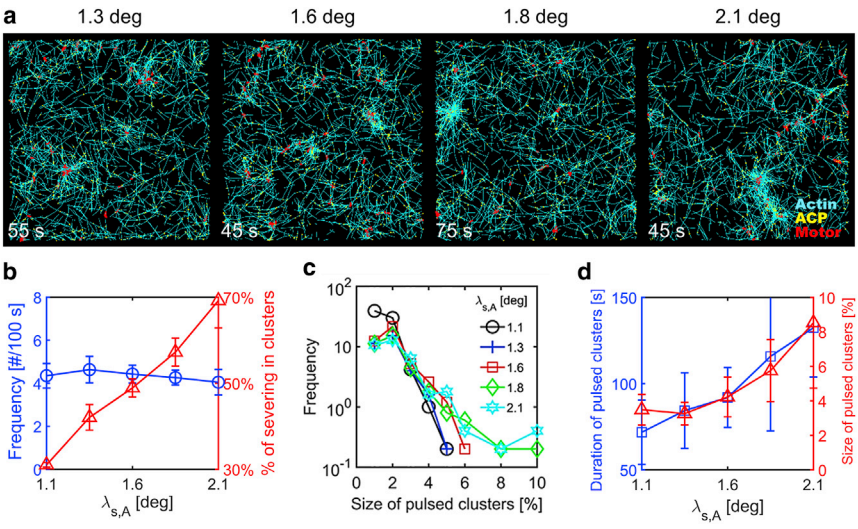

FIGURE 6 Dependence of the severing rate on a bending angle regulates the pulsed contraction. We modulated insensitivity of the severing rate to a bending angle ($\lambda_{s,A}$) at $R_M = 0.04$, $R_{ACP} = 0.02$, $<L_f> = 1$ μm, $k_{t,A} = 30$ s^{-1}, and $k^0_{s,A} = 10^{-30}$ s^{-1}. Severing takes place at larger bending angles if $\lambda_{s,A}$ is larger. (*a*) The morphology of networks with various $\lambda_{s,A}$. With higher $\lambda_{s,A}$, more large pulsed clusters emerge. (*b*) The frequency of appearance of pulsed clusters per 100 s (*blue circle*) and percentage of severing events occurring within pulsed clusters (*red triangle*) depending on $\lambda_{s,A}$. Although relatively the same number of clusters are formed regardless of $\lambda_{s,A}$, more severing events take place within clusters as $\lambda_{s,A}$ increases. (*c*) The distribution of size of pulsed clusters with different $\lambda_{s,A}$. With larger $\lambda_{s,A}$, there are a greater number of large pulsed clusters, although small pulsed clusters appear at a similar frequency. (*d*) The average duration (*blue circle*) and size (*red triangle*) of the largest pulsed clusters found from each of five simulations depending on $\lambda_{s,A}$. With larger $\lambda_{s,A}$, there are more larger clusters, and they last longer. To see this figure in color, go online.

certain morphogenetic events. Despite efforts made by a myriad of theoretical, computational, and in vitro experimental studies, critical regulators of the pulsed contraction emerging in the actomyosin cortex remain elusive. Considering that stability of actomyosin cortex is maintained by F-actin turnover, it is likely that pulsed contraction is involved with competition and balance between force generation from motors and force relaxation induced by F-actin dynamics. In this study, we employed a computational model to illuminate the origins of pulsed contraction.

First, we demonstrated that actin turnover highly affects the contractile behaviors of a network. As F-actin turns over more slowly, a network becomes more heterogeneous, with larger irreversible clusters. This is consistent with several computational studies showing the effects of F-actin turnover on contractile behaviors of networks (18–20). To correlate motor activities with a variation in network morphology, we quantified the speed and persistency of motor movements. We found that when a network forms large clusters, motors move toward the center of the clusters in a persistent manner and then slow down after reaching the center. By contrast, when cluster formation is inhibited by fast actin turnover, motors keep moving fast and less persistently. Because treadmilling occurs toward the barbed end of F-actin, it can prevent motors from stably walking for long times, causing less persistent motions.

In addition, it has been suggested that connectivity between F-actins also plays an important role for contractile behaviors of actomyosin networks. For example, an in vitro experiment using cell extracts from *Xenopus* egg cells showed that a change in the amount of one type of ACPs, α-actinin, can result in distinct morphologies in the presence of actin turnover by modulating network connectivity (42). Without actin turnover, effects of network connectivity on contractile behaviors of actomyosin networks are shown to be significant (8,10,16). We probed effects of connectivity between F-actins on network morphology and motor movements by changing either F-actin length or ACP density at relatively low actin turnover rate. At low network connectivity, the network minimally contracts or shows formation of small clusters, leading to less persistent movements of motors. An increase in network connectivity results in formation of large clusters with very persistent motor movements. Emergence of the large clusters is related to increased ranges over which forces generated by motors are transmitted (42). A further increase in network connectivity suppresses formation of separated clusters, resulting in bundled networks with less persistent motor movements. However, the entire network will contract into a single cluster at such high connectivity in the absence of the periodic boundary condition as demonstrated in a previous study (8) because the effective size of the network becomes finite without the periodic boundary condition. It is expected that the ACP density at which the network transitions between the three states (small clusters, large clusters, and bundle network) is proportional to the actin turnover rate as shown in our previous study (17). For example, if F-actin turns over faster, the transitions will occur at higher ACP density to achieve the same degree of network connectivity.

Interestingly, we found that weak pulsed contraction with nascent clusters occurs when there is subtle balance between force generation by myosin motors and force relaxation by actin turnover. These short-lived small clusters appear by themselves or in conjunction with clusters with size fluctuating over time in a very narrow parametric regime comprised of ACP density and the turnover rate and average length of F-actin. Outside the regime, most of the clusters irreversibly grow or decay very slowly after growth. None of these clusters resemble large pulsed clusters observed in cells (5,7,43). Although duration of the short-lived clusters is similar to that of the in vivo pulsed clusters ($\sim$1 min), they are much smaller in size. The fluctuating clusters show pulsed growth and shrinkage but do not disassemble completely. The decaying clusters exhibit reversibility, but they are disassembled too slowly. As mentioned earlier, using turnover of entire F-actins, a recent computational study demonstrated emergence of clusters showing pulsed behaviors (20), but they are close to fluctuating clusters rather than the in vivo pulsed clusters. All of these imply that force relaxation only via F-actin turnover is not enough to form the large distinct pulsed clusters. As size of clusters increases, more F-actins are entangled and cross-linked heavily with each other within the clusters. Then, it becomes very hard to disassemble the clusters because of very high connectivity between F-actins, resulting in very slow decay or irreversible growth. If actin turnover is very fast, disassembly of large clusters might be possible, but such large clusters are not formed because force relaxation by actin turnover dominates force generation by motors. Therefore, formation of the distinct large pulsed clusters requires an additional mechanism for locally reducing F-actin connectivity within clusters and thus relaxing forces generated by motors.

We found that angle-dependent severing of F-actin can be the additional mechanism. Buckling-induced F-actin severing has been observed during myosin-driven contraction of actin networks (14) and membrane-bound F-actins (44). Severing of F-actin can decrease network connectivity by breaking F-actin into two fragments, which may facilitate force relaxation and cluster disassembly. We demonstrated that F-actin severing enables large clusters to be disassembled quickly, resulting in a significant increase in the size and duration of the pulsed clusters. If F-actin severing tends to occur slower or at larger bending angles, a larger portion of severing events take place within the clusters, leading to the appearance of larger pulsed clusters. This indicates that F-actin severing can induce local force relaxation selectively in large clusters. However, if F-actin severing hardly occurs because of either a very low base rate or very low insensitivity to bending angles, clusters

become irreversible or decay very slowly. By contrast, if severing occurs too frequently, a significant reduction in filament length prevents F-actins from forming large clusters. In addition, we found that formation of large pulsed clusters requires both F-actin severing and actin turnover via treadmilling. If treadmilling does not occur (i.e., without actin polymerization or depolymerization), fragmented filaments resulting from severing cannot be completely depolymerized or elongated. As a result, F-actin length is reduced significantly, so cluster formation does not occur.

Cells have various ways to regulate the severing rate of F-actins. The activity of gelsolin, which severs F-actin by destabilizing interactions between actins and then binds to a new barbed end, is regulated by Ca^{2+} (45). In addition, previous studies have shown that binding of cofilin to F-actin promotes severing (30,46). Depending on cofilin concentration, severing events occur with quite distinct rates and different angle insensitivities. Association of cofilin to F-actin can be enhanced significantly by diverse actin-binding proteins, such as coronin and Aip 1 (47,48). Therefore, variations in parameters for the F-actin severing rate in this study may be related to physiological functions of cells.

Recent experiments have demonstrated that pulsed contraction results from contractile instability regulated by spatiotemporal expression of RhoA (36,40,41,43). During morphogenetic events and in the one-cell-stage *C. elegans* embryo, myosin and RhoA colocalize with the pulsed clusters. Although results from those experiments have suggested that the pulsed contraction is a direct consequence of RhoA cycling activity (40), a recent study suggested that RhoA might act as a pacemaker (36). During one pulse, RhoA locally enhances activities of myosin motors to form clusters and then deactivate the motors later. However, after deactivation of motor activities, it is not likely that numerous connections between F-actins within clusters are broken simultaneously for disassembly of the clusters. Based on the results in our study, it is anticipated that the turnover and severing of F-actin still play a very crucial role for cluster disassembly and pulsed contraction by locally reducing connectivity within the clusters.

Thus, our study provides insights into understanding of a role of F-actin severing for the distinct pulsed contraction observed during various physiological events. In our future studies, we will incorporate the spatiotemporal expression of RhoA and then relate the RhoA activity with motor activities to recapitulate and study more physiological pulsed contraction.

SUPPORTING MATERIAL

Supporting Materials and Methods, nine figures, one table, and five videos are available at http://www.biophysj.org/biophysj/supplemental/S0006-3495(18)31154-8.

AUTHOR CONTRIBUTIONS

Q.Y. and J.L. performed simulations and analysis. J.L., Q.Y., and T.K. designed the research. J.L., Q.Y., M.P.M., and T.K. wrote the manuscript. T.K. provided the software and computational resources.

ACKNOWLEDGMENTS

The authors gratefully acknowledge the support from the National Institutes of Health (1R01GM126256) and the support of the Indiana Clinical and Translational Sciences Institute (UL1TR001108) from the National Institutes of Health, National Center for Advancing Translational Sciences, Clinical and Translational Sciences Award.

SUPPORTING CITATIONS

References (49–57) appear in the Supporting Material.

REFERENCES

1. Lim, C. T., E. H. Zhou, and S. T. Quek. 2006. Mechanical models for living cells–a review. *J. Biomech.* 39:195–216.
2. Salbreux, G., G. Charras, and E. Paluch. 2012. Actin cortex mechanics and cellular morphogenesis. *Trends Cell Biol.* 22:536–545.
3. Murrell, M., P. W. Oakes, …, M. L. Gardel. 2015. Forcing cells into shape: the mechanics of actomyosin contractility. *Nat. Rev. Mol. Cell Biol.* 16:486–498.
4. Eggert, U. S., T. J. Mitchison, and C. M. Field. 2006. Animal cytokinesis: from parts list to mechanisms. *Annu. Rev. Biochem.* 75:543–566.
5. Munro, E., J. Nance, and J. R. Priess. 2004. Cortical flows powered by asymmetrical contraction transport PAR proteins to establish and maintain anterior-posterior polarity in the early C. elegans embryo. *Dev. Cell.* 7:413–424.
6. Leptin, M. 2005. Gastrulation movements: the logic and the nuts and bolts. *Dev. Cell.* 8:305–320.
7. Martin, A. C., M. Kaschube, and E. F. Wieschaus. 2009. Pulsed contractions of an actin-myosin network drive apical constriction. *Nature.* 457:495–499.
8. Alvarado, J., M. Sheinman, …, G. H. Koenderink. 2013. Molecular motors robustly drive active gels to a critically connected state. *Nat. Phys.* 9:591–597.
9. Bois, J. S., F. Jülicher, and S. W. Grill. 2011. Pattern formation in active fluids. *Phys. Rev. Lett.* 106:028103.
10. Ennomani, H., G. Letort, …, L. Blanchoin. 2016. Architecture and connectivity govern actin network contractility. *Curr. Biol.* 26:616–626.
11. Reymann, A. C., R. Boujemaa-Paterski, …, L. Blanchoin. 2012. Actin network architecture can determine myosin motor activity. *Science.* 336:1310–1314.
12. Jung, W., M. P. Murrell, and T. Kim. 2015. F-actin cross-linking enhances the stability of force generation in disordered actomyosin networks. *Comput. Part. Mech.* 2:317–327.
13. Oelz, D. 2014. A viscous two-phase model for contractile actomyosin bundles. *J. Math. Biol.* 68:1653–1676.
14. Murrell, M. P., and M. L. Gardel. 2012. F-actin buckling coordinates contractility and severing in a biomimetic actomyosin cortex. *Proc. Natl. Acad. Sci. USA.* 109:20820–20825.
15. Lenz, M., T. Thoresen, …, A. R. Dinner. 2012. Contractile units in disordered actomyosin bundles arise from F-actin buckling. *Phys. Rev. Lett.* 108:238107.
16. Li, J., T. Biel, …, T. Kim. 2017. Buckling-induced F-actin fragmentation modulates the contraction of active cytoskeletal networks. *Soft Matter.* 13:3213–3220.

17. Mak, M., M. H. Zaman, …, T. Kim. 2016. Interplay of active processes modulates tension and drives phase transition in self-renewing, motor-driven cytoskeletal networks. *Nat. Commun.* 7:10323.
18. Hiraiwa, T., and G. Salbreux. 2016. Role of turnover in active stress generation in a filament network. *Phys. Rev. Lett.* 116:188101.
19. McFadden, W. M., P. M. McCall, …, E. M. Munro. 2017. Filament turnover tunes both force generation and dissipation to control long-range flows in a model actomyosin cortex. *PLoS Comput. Biol.* 13:e1005811.
20. Belmonte, J. M., M. Leptin, and F. Nédélec. 2017. A theory that predicts behaviors of disordered cytoskeletal networks. *Mol. Syst. Biol.* 13:941.
21. Kim, T., W. Hwang, …, R. D. Kamm. 2009. Computational analysis of viscoelastic properties of crosslinked actin networks. *PLoS Comput. Biol.* 5:e1000439.
22. Underhill, P. T., and P. S. Doyle. 2004. On the coarse-graining of polymers into bead-spring chains. *J. Non-Newt. Fluid Mech.* 122:3–31.
23. Bell, G. I. 1978. Models for the specific adhesion of cells to cells. *Science.* 200:618–627.
24. Erdmann, T., and U. S. Schwarz. 2012. Stochastic force generation by small ensembles of myosin II motors. *Phys. Rev. Lett.* 108:188101.
25. Erdmann, T., P. J. Albert, and U. S. Schwarz. 2013. Stochastic dynamics of small ensembles of non-processive molecular motors: the parallel cluster model. *J. Chem. Phys.* 139:175104.
26. Kasza, K. E., C. P. Broedersz, …, D. A. Weitz. 2010. Actin filament length tunes elasticity of flexibly cross-linked actin networks. *Biophys. J.* 99:1091–1100.
27. Koenderink, G. H., Z. Dogic, …, D. A. Weitz. 2009. An active biopolymer network controlled by molecular motors. *Proc. Natl. Acad. Sci. USA.* 106:15192–15197.
28. Chugh, P., A. G. Clark, …, E. K. Paluch. 2017. Actin cortex architecture regulates cell surface tension. *Nat. Cell Biol.* 19:689–697.
29. Erlenkämper, C., and K. Kruse. 2013. Treadmilling and length distributions of active polar filaments. *J. Chem. Phys.* 139:164907.
30. McCullough, B. R., E. E. Grintsevich, …, E. M. De La Cruz. 2011. Cofilin-linked changes in actin filament flexibility promote severing. *Biophys. J.* 101:151–159.
31. Freedman, S. L., S. Banerjee, …, A. R. Dinner. 2017. A versatile framework for simulating the dynamic mechanical structure of cytoskeletal networks. *Biophys. J.* 113:448–460.
32. Dierkes, K., A. Sumi, …, G. Salbreux. 2014. Spontaneous oscillations of elastic contractile materials with turnover. *Phys. Rev. Lett.* 113:148102.
33. Machado, P. F., G. B. Blanchard, …, N. Gorfinkiel. 2014. Cytoskeletal turnover and myosin contractility drive cell autonomous oscillations in a model of Drosophila dorsal closure. *Eur. Phys. J. Spec. Top.* 223:1391–1402.
34. Hannezo, E., B. Dong, …, S. Hayashi. 2015. Cortical instability drives periodic supracellular actin pattern formation in epithelial tubes. *Proc. Natl. Acad. Sci. USA.* 112:8620–8625.
35. Bendix, P. M., G. H. Koenderink, …, D. A. Weitz. 2008. A quantitative analysis of contractility in active cytoskeletal protein networks. *Biophys. J.* 94:3126–3136.
36. Nishikawa, M., S. R. Naganathan, …, S. W. Grill. 2017. Controlling contractile instabilities in the actomyosin cortex. *eLife.* 6:e19595.
37. Cooper, J. A. 1987. Effects of cytochalasin and phalloidin on actin. *J. Cell Biol.* 105:1473–1478.
38. Wakatsuki, T., B. Schwab, …, E. L. Elson. 2001. Effects of cytochalasin D and latrunculin B on mechanical properties of cells. *J. Cell Sci.* 114:1025–1036.
39. Kraning-Rush, C. M., S. P. Carey, …, C. A. Reinhart-King. 2011. The role of the cytoskeleton in cellular force generation in 2D and 3D environments. *Phys. Biol.* 8:015009.
40. Mason, F. M., S. Xie, …, A. C. Martin. 2016. RhoA GTPase inhibition organizes contraction during epithelial morphogenesis. *J. Cell Biol.* 214:603–617.
41. Vasquez, C. G., M. Tworoger, and A. C. Martin. 2014. Dynamic myosin phosphorylation regulates contractile pulses and tissue integrity during epithelial morphogenesis. *J. Cell Biol.* 206:435–450.
42. Tan, T. H., M. Malik-Garbi, …, N. Fakhri. 2018. Self-organized stress patterns drive state transitions in actin cortices. *Sci. Adv.* 4:eaar2847.
43. Baird, M. A., N. Billington, …, C. M. Waterman. 2017. Local pulsatile contractions are an intrinsic property of the myosin 2A motor in the cortical cytoskeleton of adherent cells. *Mol. Biol. Cell.* 28:240–251.
44. Vogel, S. K., Z. Petrasek, …, P. Schwille. 2013. Myosin motors fragment and compact membrane-bound actin filaments. *eLife.* 2:e00116.
45. Yin, H. L. 1987. Gelsolin: calcium- and polyphosphoinositide-regulated actin-modulating protein. *BioEssays.* 7:176–179.
46. Elam, W. A., H. Kang, and E. M. De la Cruz. 2013. Biophysics of actin filament severing by cofilin. *FEBS Lett.* 587:1215–1219.
47. Chen, Q., N. Courtemanche, and T. D. Pollard. 2015. Aip1 promotes actin filament severing by cofilin and regulates constriction of the cytokinetic contractile ring. *J. Biol. Chem.* 290:2289–2300.
48. Mikati, M. A., D. Breitsprecher, …, B. L. Goode. 2015. Coronin enhances actin filament severing by recruiting cofilin to filament sides and altering F-actin conformation. *J. Mol. Biol.* 427:3137–3147.
49. Tyska, M. J., D. E. Dupuis, …, S. Lowey. 1999. Two heads of myosin are better than one for generating force and motion. *Proc. Natl. Acad. Sci. USA.* 96:4402–4407.
50. Clift, R., J. R. Grace, and M. E. Weber. 2005. Bubbles, Drops, and Particles. Courier Corporation, North Chelmsford, MA.
51. Isambert, H., P. Venier, …, M. F. Carlier. 1995. Flexibility of actin filaments derived from thermal fluctuations. Effect of bound nucleotide, phalloidin, and muscle regulatory proteins. *J. Biol. Chem.* 270:11437–11444.
52. Ferrer, J. M., H. Lee, …, M. J. Lang. 2008. Measuring molecular rupture forces between single actin filaments and actin-binding proteins. *Proc. Natl. Acad. Sci. USA.* 105:9221–9226.
53. Kim, T. 2015. Determinants of contractile forces generated in disorganized actomyosin bundles. *Biomech. Model. Mechanobiol.* 14:345–355.
54. Jung, W., M. P. Murrell, and T. Kim. 2016. F-actin fragmentation induces distinct mechanisms of stress relaxation in the actin cytoskeleton. *ACS Macro Lett.* 5:641–645.
55. Wioland, H., A. Jegou, and G. Romet-Lemonne. 2018. Torsional stress generated by ADF/cofilin on cross-linked actin filaments boosts their severing. *bioRXiv* https://doi.org/10.1101/380113.
56. Kishino, A., and T. Yanagida. 1988. Force measurements by micromanipulation of a single actin filament by glass needles. *Nature.* 334:74–76.
57. Meyer, R. K., and U. Aebi. 1990. Bundling of actin filaments by alpha-actinin depends on its molecular length. *J. Cell Biol.* 110:2013–2024.

Biophysical Journal, Volume *115*

Supplemental Information

Balance between Force Generation and Relaxation Leads to Pulsed Contraction of Actomyosin Networks

Qilin Yu, Jing Li, Michael P. Murrell, and Taeyoon Kim

SUPPLEMENTAL INFORMATION

Brownian dynamics via the Langevin equation

In our agent-based model, F-actins consist of serially connected cylindrical segments with polarity: barbed and pointed ends. Actin cross-linking proteins (ACPs) are comprised of a pair of cylindrical segments. Each motor is modeled to mimic geometry of myosin thick filaments; each motor has a backbone structure with four arms ($N_a = 4$), and each of the arms represents 8 myosin heads ($N_h = 8$). Thus, the total number of myosin heads represented by one motor is 32, which is not very different from 56 myosin heads in one non-muscle myosin thick filament (1). Displacements of the segments are determined by the Langevin equation with negligence of inertia:

$$\mathbf{F}_i - \zeta_i \frac{\mathrm{d}\mathbf{r}_i}{\mathrm{d}t} + \mathbf{F}_i^{\mathrm{T}} = 0 \tag{S1}$$

where $\mathbf{r}_i$ is a position vector of the ith element, ζ_i is a drag coefficient, t is time, $\mathbf{F}_i$ is deterministic force, and $\mathbf{F}_i^{\mathrm{T}}$ is a stochastic force satisfying the fluctuation-dissipation theorem (2):

$$\left\langle \mathbf{F}_i^{\mathrm{T}}(t)\mathbf{F}_j^{\mathrm{T}}(t) \right\rangle = \frac{2k_{\mathrm{B}}T\zeta_i\delta_{ij}}{\Delta t}\boldsymbol{\delta} \tag{S2}$$

where $\boldsymbol{\delta}$ is a second-order tensor, δ_{ij} is the Kronecker delta, and $\Delta t = 1.15 \times 10^{-5}$ s is a time step. Drag coefficients are computed using an approximated form for a cylindrical object (3):

$$\zeta_i = 3\pi\mu r_{\mathrm{c},i}\frac{3 + 2r_{0,i}/r_{\mathrm{c},i}}{5} \tag{S3}$$

where μ is viscosity of surrounding medium, and $r_{0,i}$ and $r_{\mathrm{c},i}$ are length and diameter of a segment, respectively. Positions of all the cylindrical segments are updated every time step using the Euler integration scheme:

$$\mathbf{r}_i(t + \Delta t) = \mathbf{r}_i(t) + \frac{\mathrm{d}\mathbf{r}_i}{\mathrm{d}t}\Delta t = \mathbf{r}_i(t) + \frac{1}{\zeta_i}\left(\mathbf{F}_i + \mathbf{F}_i^{\mathrm{T}}\right)\Delta t \tag{S4}$$

Deterministic forces

Deterministic forces include extensional forces maintaining equilibrium lengths, bending forces maintaining equilibrium angles, and repulsive forces accounting for volume-exclusion effects between actin segments. The extensional and bending forces originate from the following potentials:

$$U_{\mathrm{s}} = \frac{1}{2}\kappa_{\mathrm{s}}(r - r_0)^2 \tag{S5}$$

$$U_{\mathrm{b}} = \frac{1}{2}\kappa_{\mathrm{b}}\left(\theta - \theta_0\right)^2 \tag{S6}$$

where κ_{s} and κ_{b} are extensional and bending stiffnesses, r and r_0 is instantaneous and equilibrium lengths of cylindrical segments, and θ and θ_0 are instantaneous and equilibrium angles formed by adjacent segments. An equilibrium length of actin segments ($r_{0,\mathrm{A}}$ = 140 nm) and an equilibrium angle formed by two adjacent actin segments ($\theta_{0,\mathrm{A}}$ = 0 rad) are maintained by extensional ($\kappa_{\mathrm{s,A}}$) and bending stiffnesses of actins ($\kappa_{\mathrm{b,A}}$), respectively. The reference value of $\kappa_{\mathrm{b,A}}$ corresponds to the persistence length of 9 μm (4). An equilibrium length of ACP arms ($r_{0,\mathrm{ACP}}$ = 23.5 nm) and an equilibrium angle formed by two arms of each ACP ($\theta_{0,\mathrm{ACP}}$ = 0 rad) are regulated by extensional ($\kappa_{\mathrm{s,ACP}}$) and bending stiffnesses of ACPs ($\kappa_{\mathrm{b,ACP}}$), respectively. An equilibrium length of motor backbone segments ($r_{\mathrm{s,M1}}$= 42 nm) and an equilibrium angle formed by adjacent backbone segments ($\theta_{0,\mathrm{M}}$ = 0 rad) are maintained by extensional ($\kappa_{\mathrm{s,M1}}$) and bending stiffnesses ($\kappa_{\mathrm{b,M}}$), respectively. The value of $\kappa_{\mathrm{s,M1}}$ is equal to that of $\kappa_{\mathrm{s,A}}$, whereas the value of $\kappa_{\mathrm{b,M}}$ is larger than that of $\kappa_{\mathrm{b,A}}$. Extension of each motor arm is regulated by the two-spring model with stiffnesses of transverse ($\kappa_{\mathrm{s,M2}}$) and longitudinal springs ($\kappa_{\mathrm{s,M3}}$). The transverse spring maintains an equilibrium distance ($r_{0,\mathrm{M2}}$ = 13.5 nm) between an endpoint of a motor backbone and actin segment where the arm of the motor binds, whereas the longitudinal spring helps maintain a right angle between the motor arm and the actin segment ($r_{0,\mathrm{M3}}$ = 0 nm).

Repulsive force is represented by a harmonic potential (5):

$$U_{\mathrm{r}} = \begin{cases} \dfrac{1}{2}\kappa_{\mathrm{r}}\left(r_{12} - r_{\mathrm{c,A}}\right)^2 & \text{if} \quad r_{12} < r_{\mathrm{c,A}} \\ 0 & \text{if} \quad r_{12} \geq r_{\mathrm{c,A}} \end{cases} \tag{S7}$$

where κ_r is strength of repulsive force, and r_{12} is the minimum distance between two actin segments. Forces exerted on actin segments by bound ACPs and motors or by the repulsive force are distributed onto the barbed and pointed ends of the actin segments as described in our previous work (6).

Dynamics of ACPs

ACPs bind to binding sites located on actin segments every 7 nm with no preference of contact angle at a constant rate. ACPs also unbind from F-actin in a force-dependent manner following Bell's equation (7):

$$k_{u,ACP} = \begin{cases} k^0_{u,ACP} \exp\left(\dfrac{x_{u,ACP} \left| \vec{F}_{s,ACP} \right|}{k_B T} \right) & \text{if } r \geq r_{0,ACP} \\ k^0_{u,ACP} & \text{if } r < r_{0,ACP} \end{cases} \quad \text{(S8)}$$

where $\left| \vec{F}_{s,ACP} \right|$ is spring force exerted on an ACP arm, $k^0_{u,ACP}$ is the zero-force unbinding rate constant, $x_{u,ACP}$ is sensitivity to applied force, and $k_B T$ is thermal energy. Values of $k^0_{u,ACP}$ (= 0.115 s^{-1}) and $x_{u,ACP}$ (= 1.04×10^{-10} m) are determined based on filamin A (8).

Dynamics of motors

Motor arms bind to binding sites on actin segments at a rate of $40N_h$ s^{-1}, where N_h = 8 is the number of myosin heads represented by each motor arm. Walking ($k_{w,M}$) and unbinding rates ($k_{u,M}$) of the motor arms are determined by the parallel cluster model to mimic the mechanochemical cycle of non-muscle myosin II (9, 10). Details of implementation and benchmarking of the parallel cluster model in our models are extensively described in our previous study (11). Note that $k_{w,M}$ and $k_{u,M}$ are lower with higher applied load since motors exhibit a catch-bond behavior. Unloaded walking velocity and stall force of motors are set to ~140 nm/s and ~5.7 pN, respectively.

Justification and limitation of an empirical equation for F-actin severing

Eq. 1 describes the relationship between the severing rate ($k_{s,A}$) and the sum of bending angles at two ends of each actin segment ($\theta_{s,A}$). We determined this relationship in an empirical fashion as shown in our previous study (12). An intro experiment showed that F-actin severing occurs only at relatively large bending angles ($57 \pm 9^\circ$) during thermal fluctuation (13). To mimic the experiment, we ran a simulation only with F-actins and measured bending angles of thermally fluctuating F-actins. We found that the probability of occurrence of a bending angle exponentially decreases as the angle is greater. This implies that $k_{s,A}$ needs to be extremely sensitive to an increase in the bending angle in order to let severing events occur only at large bending angles. Thus, we assumed that $k_{s,A}$ exponentially increases as the bending angle increases (Eq. 1). As a result, values of $k_{s,A}^0$ used in this study may seem unrealistically small at a glance, but such small values are necessary. The reference value of λ_{sev} = 1.6 deg was determined by comparing the distribution of bending angles where severing occurred in the simulations with the experimental observation (13). A variation in $k_{s,A}^0$ does not affect the distribution of severing angles, but as $k_{s,A}^0$ is greater, severing events occur more frequently at all bending angles.

Although we devised the relationship by comparing with experimental results, we admit that this relationship may not reflect severing dynamics very rigorously and have some limitations. For determination of $k_{s,A}$, we used bending angles rather than the radius of curvature. In the in vitro experiments, it was observed that F-actin can often be bent in a non-uniform manner with a kink, and severing is more likely to occur near the kink (13, 14). Thus, they showed a relationship between the severing rate and a bending angle rather than the radius of

curvature. This indicates that the angle-dependent severing rate could be a better way to describe the F-actin severing induced by non-uniform bending. Since we used bending angles for determining $k_{s,A}$, it is possible that parameter values inducing pulsed contraction may vary depending on how F-actin is discretized into serially-connected cylindrical segments. However, when we reduced the length of actin cylindrical segments from 140 nm to 70 nm, pulsed contraction still took place with similar parameter values (Figs. 9a, b). This implies that F-actins in our simulations undergo non-uniform deformation induced by motor activities. (i.e. more bending on a certain part of F-actin than other parts) Since F-actin severing is simulated by disappearance of one actin segment, we used the sum of two bending angles because an increase in either of the angles would lead to the severing event on the segment.

We also tried to let the F-actin severing occur deterministically; severing immediately occurs at a bending angle greater than a critical angle, whereas severing never occurs below the critical angle. We observed that distinct pulsed contraction still emerged with such a deterministic relationship (Figs. S9c, d). This implies that emergence of pulsed contraction due to balance between force generation and global/local force relaxation is not sensitive to the choice of a specific model for F-actin severing. As long as F-actin severing occurs selectively at large angles, the pulsed contraction can be reproduced. Note that we do not try to find universal parameter values for pulsed contraction that work with any assumption. Our aim in this study is to provide insights into a possible mechanical mechanism for pulsed contraction observed in cells by showing that F-actin severing induced by buckling can drive the pulsed contraction via local force relaxation. Predictions from our computational study are rather qualitative, not very quantitative, due to uncertainty and limitations of the F-actin severing although our model reflects the treadmilling and severing of F-actins more accurately than previous models.

Determination of threshold values for quantification of the clustering behaviors

As explained in the main text, we used a threshold value for detection of clusters. Depending on the threshold value, results of the analysis can vary substantially. If the value is very low, the analysis method will detect too many trivial structures that are too small to be considered clusters. By contrast, if the value is too high, only very large clusters will be detected. Thus, the threshold value should be chosen carefully. To find an optimal value, we analyzed clustering behaviors in several cases. As examples, we show fluctuation of the actin density in all grids for 200 s under three conditions: (i) a network with a high treadmilling rate (120 s^{-1}), (ii) a network without motors, and (iii) a network with an intermediate treadmilling rate. The first and second cases show negligible contraction due to either very high force relaxation or very low force generation. All grids in the first and second cases exhibit only small fluctuation with a few small peaks (Figs. S8d, e, g, h). Peak actin density in each grid has an average value between 11 to 12 (Figs. S8a, b). All the peaks last for less than 20 s, so these peaks cannot represent significant clustering behaviors. However, the third case, with higher average density (Fig. S8c), shows distinct peaks whose density and duration are much larger than small fluctuation (Figs. S8f, i), and nascent pulsed clusters are clearly observed in network morphology. To capture the nascent pulsed clusters but ignore small peaks, we set the threshold value for density to be 12. Additionally, we set a threshold value for duration to be 20 s. The combination of the spatial and temporal threshold values enables us to detect most of the statistically significant clusters in a network. In a homogenous network, such combination prevents background fluctuations from being detected as nascent pulsed clusters (Fig. S8j).

Table S1. List of parameters employed in the model. For some of the parameters, references are provided if the parameters were determined based on specific previous studies.

Symbol	Definition	Value
$r_{0,A}$	Length of an actin segment	1.4×10^{-7} or 0.7×10^{-7} [m]
$r_{c,A}$	Diameter of an actin segment	7.0×10^{-9} [m] (15)
$\theta_{0,A}$	Bending angle formed by adjacent actin segments	0 [rad]
$\kappa_{s,A}$	Extensional stiffness of F-actin	1.69×10^{-2} [N/m]
$\kappa_{b,A}$	Bending stiffness of F-actin	2.64×10^{-19} [N·m] (4)
$r_{0,ACP}$	Length of an ACP arm	2.35×10^{-8} [m] (16)
$r_{c,ACP}$	Diameter of an ACP arm	1.0×10^{-8} [m]
$\theta_{0,ACP}$	Bending angle formed by two ACP arms	0 [rad]
$\kappa_{s,ACP}$	Extensional stiffness of ACP	2.0×10^{-3} [N/m]
$\kappa_{b,ACP}$	Bending stiffness of ACP	1.04×10^{-19} [N·m]
$r_{0,M1}$	Length of a motor backbone segment	4.2×10^{-8} [m]
$r_{0,M2}$	Length of a motor arm	1.35×10^{-8} [m]
$r_{c,M}$	Diameter of a motor arm	1.0×10^{-8} [m]
$\theta_{0,M}$	Bending angle formed by motor backbone segments	0 [rad]
$\kappa_{s,M1}$	Extensional stiffness of a motor backbone	1.69×10^{-2} [N/m]
$\kappa_{s,M2}$	Extensional stiffness 1 of a motor arm	1.0×10^{-3} [N/m]
$\kappa_{s,M3}$	Extensional stiffness 2 of a motor arm	1.0×10^{-3} [N/m]
$\kappa_{b,M}$	Bending stiffness of a motor backbone	5.07×10^{-18} [N·m]
N_h	Number of heads represented by a motor arm	8
N_a	Number of arms per motor	4
$k_{n,A}$	Nucleation rate of actin	0.0225 – 0.36 [$\mu M^{-1}s^{-1}$]
$k_{+,A}$	Polymerization rate of actin at the barbed end	15 - 240 [$\mu M^{-1}s^{-1}$]
$k_{-,A}$	Depolymerization rate of actin at the pointed end	15 - 240 [s^{-1}]
$k_{s,A}^0$	Zero-angle severing rate constant	10^{-60} – 10^{-10} [s^{-1}]
$\lambda_{s,A}$	Insensitivity of a severing rate to a bending angle	0.3 – 2.9 [deg]
$k_{u,ACP}^0$	Zero-force unbinding rate constant of ACP	0.115 [s^{-1}] (8)
$x_{u,ACP}$	Sensitivity of ACP unbinding to applied force	1.04×10^{-10} [m] (8)
κ_r	Strength of repulsive force	1.69×10^{-3} [N/m]
Δt	Time step	1.15×10^{-5} [s]
μ	Viscosity of surrounding medium	8.6×10^{-1} [kg/m·s]
k_BT	Thermal energy	4.142×10^{-21} [J]
C_A	Actin concentration	60 [μM]
R_M	Ratio of motor concentration to C_A	0.04
R_{ACP}	Ratio of ACP concentration to C_A	0.0025-0.16
$<L_f>$	Average length of F-actins	0.7 – 5.0 [μm]

SUPPLEMENTAL FIGURES

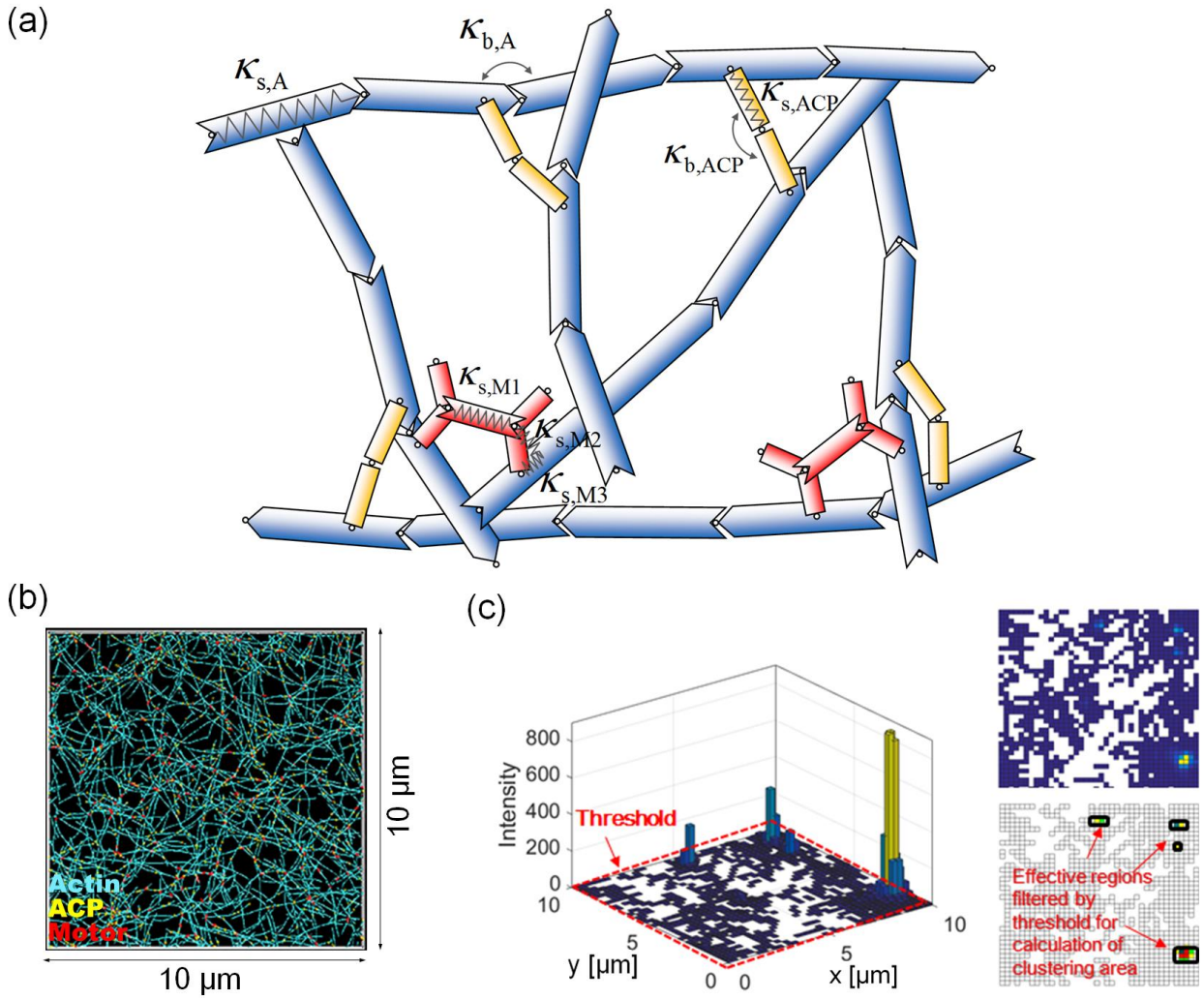

Figure S1. Model and analysis used in the study. (a) A schematic diagram showing an actomyosin network consisting of F-actin (cyan), actin crosslinking protein (yellow), and motor (red). These three elements are simplified by cylindrical segments. Equilibrium lengths of segments and equilibrium angles formed by adjacent segments are maintained by extensional stiffness (κ_s) and bending stiffness (κ_b), respectively. (b) An example of a network in a thin computational domain ($10 \times 10 \times 0.1$ μm). (c) Quantification of clusters based on actin density. A 3D histogram at each time point is created using density of actin segments. Then, adjacent regions whose actin density is above a certain threshold are considered one cluster. This analysis is repeated for all time points, and then clusters at two consecutive time points are correlated using criteria explained in the text.

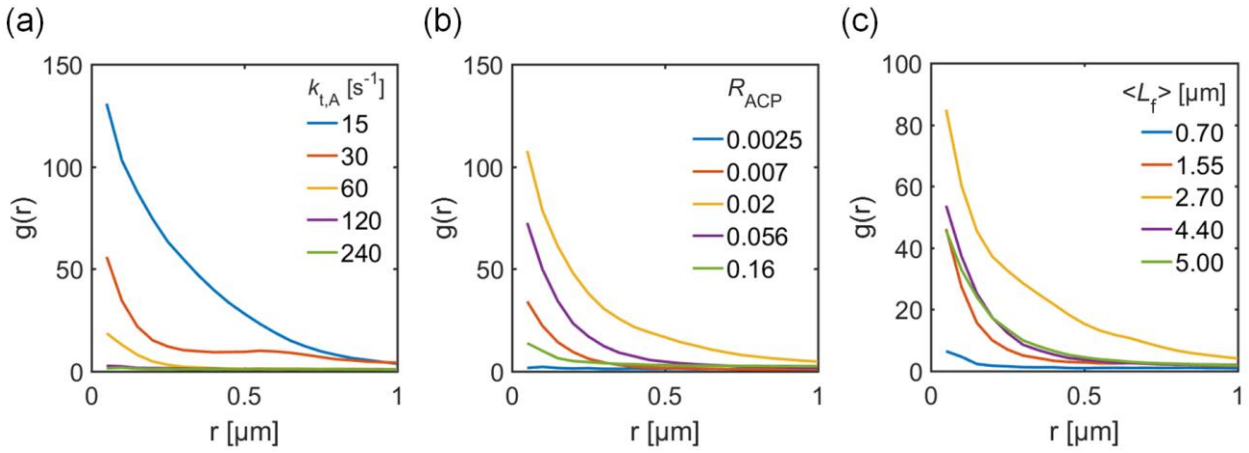

Figure S2. Radial distribution function as an additional measure for network heterogeneity. (a) Cases with various treadmilling rates shown in Fig. 1. (b) Cases with five different ACP density shown in Fig. 2. (c) Cases with five average F-actin lengths shown in Fig. 3. Higher values of $g(r)$ at smaller r indicate more heterogeneous network morphology.

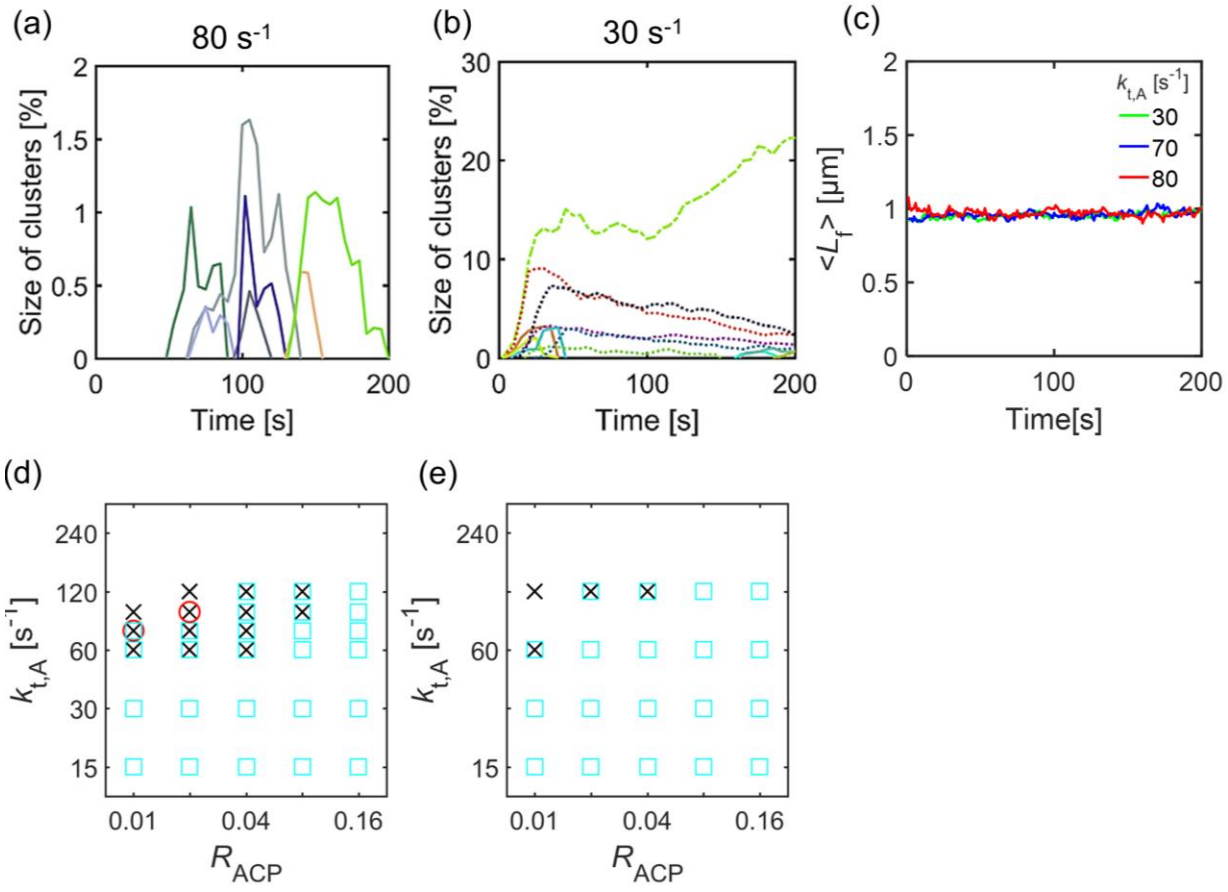

Figure S3. Examples of simulations showing small pulsed, fluctuating, decaying, and growing clusters. $k_{t,A}$ is set to be 30, 70 or 80 s^{-1} at R_M = 0.04, R_{ACP} = 0.01, and $<L_f>$ = 1 μm. (a, b) Time evolution of percentage of actin segments located within all identified clusters with two different $k_{t,A}$. Random colors are assigned to curves to distinguish each cluster. Pulsed, decaying, and irreversible (fluctuating and growing) clusters are shown by solid, dotted, and dot-dashed lines, respectively. In (a), only small pulsed clusters appear. In (b), decaying and growing clusters are formed. Some small clusters still form but disassemble very rapidly at early times. (c) Time evolution of average length of F-actins ($<L_f>$) for two cases shown in (a-b) and one case shown in Fig. 4d. (d, e) Phase diagrams summarizing types of clusters emerging under various conditions of $k_{t,A}$ and R_{ACP} for (d) $<L_f>$ = 1 μm and (e) $<L_f>$ = 1.6 μm. Red circle, black cross, and cyan square represent fluctuating cluster, small pulsatile cluster, and irreversible/decaying cluster, respectively.

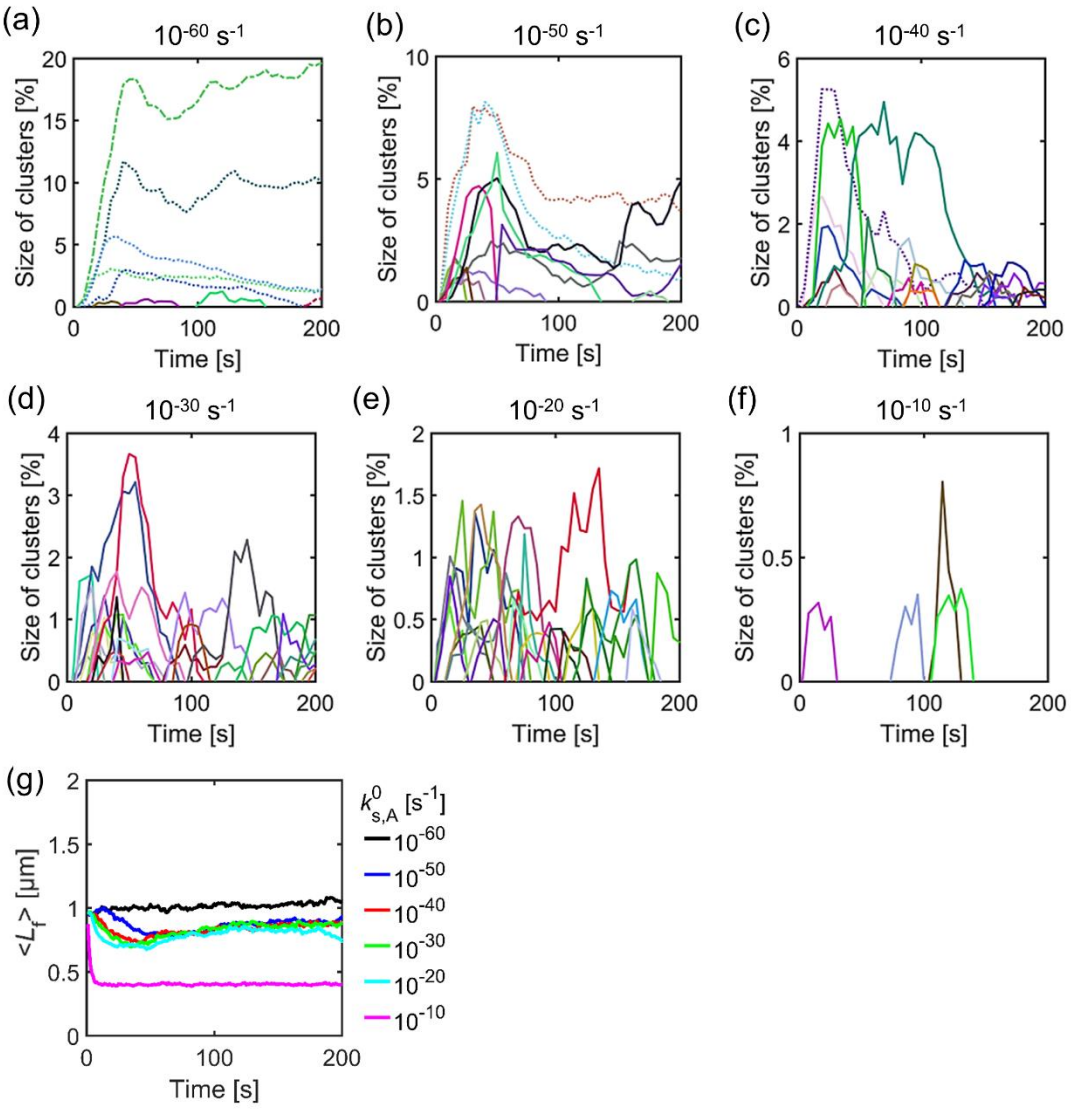

Figure S4. Effects of the zero-angle severing rate constant ($k^0_{s,A}$). Cases shown here are the same as those shown in Fig. 5. We varied $k^0_{s,A}$ between 10^{-60} s^{-1} and 10^{-10} s^{-1} at R_M = 0.04, R_{ACP} = 0.02, and $k_{t,A}$ = 30 s^{-1}. (a-f) Time evolution of percentage of actin segments located within all identified clusters. Random colors are used for curves to distinguish each cluster. Pulsed, decaying, and irreversible (fluctuating and growing) clusters are represented by solid, dotted, and dot-dashed lines, respectively. (g) Time evolution of average length of F-actins (<L_f>) for 6 cases shown in (a-f). An increase in $k^0_{s,A}$ does not shorten F-actins much in most cases except a case with $k^0_{s,A}$ = 10^{-10} s^{-1}.

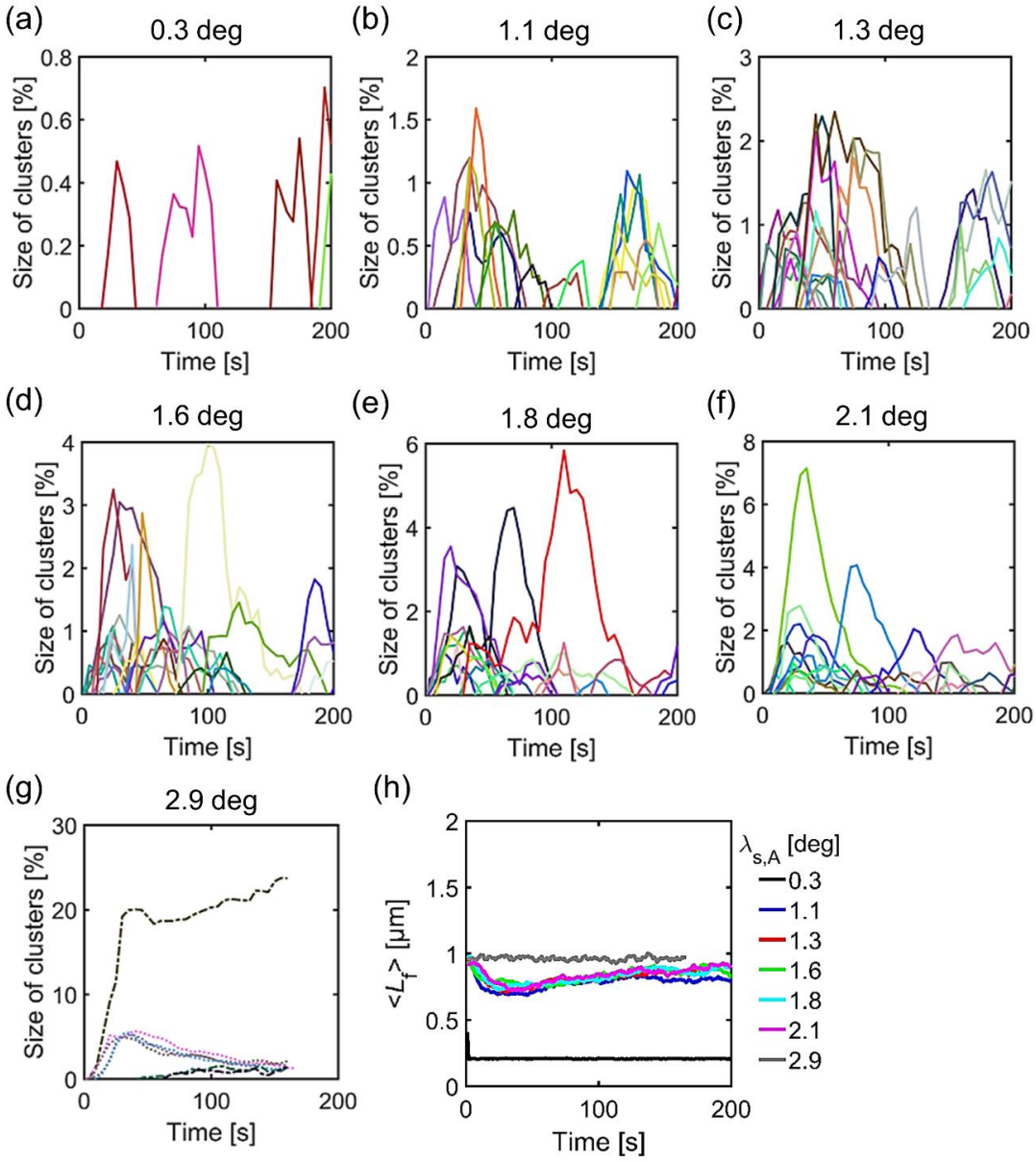

Figure S5. Impacts of insensitivity of severing to a bending angle ($\lambda_{s,A}$). Cases shown here are the same as those shown in Fig. 6. (a-g) Time evolution of percentage of actins located within all identified clusters. Random colors are assigned to curves to distinguish each cluster. Pulsed, decaying, and irreversible (fluctuating and growing) clusters are shown by solid, dotted, and dot-dashed lines, respectively. (h) Time evolution of average length of F-actins ($<L_f>$) for 7 cases shown in (a-g). A change in $\lambda_{s,A}$ does not affect $<L_f>$ significantly except in a case with $\lambda_{s,A}$ = 0.3 deg.

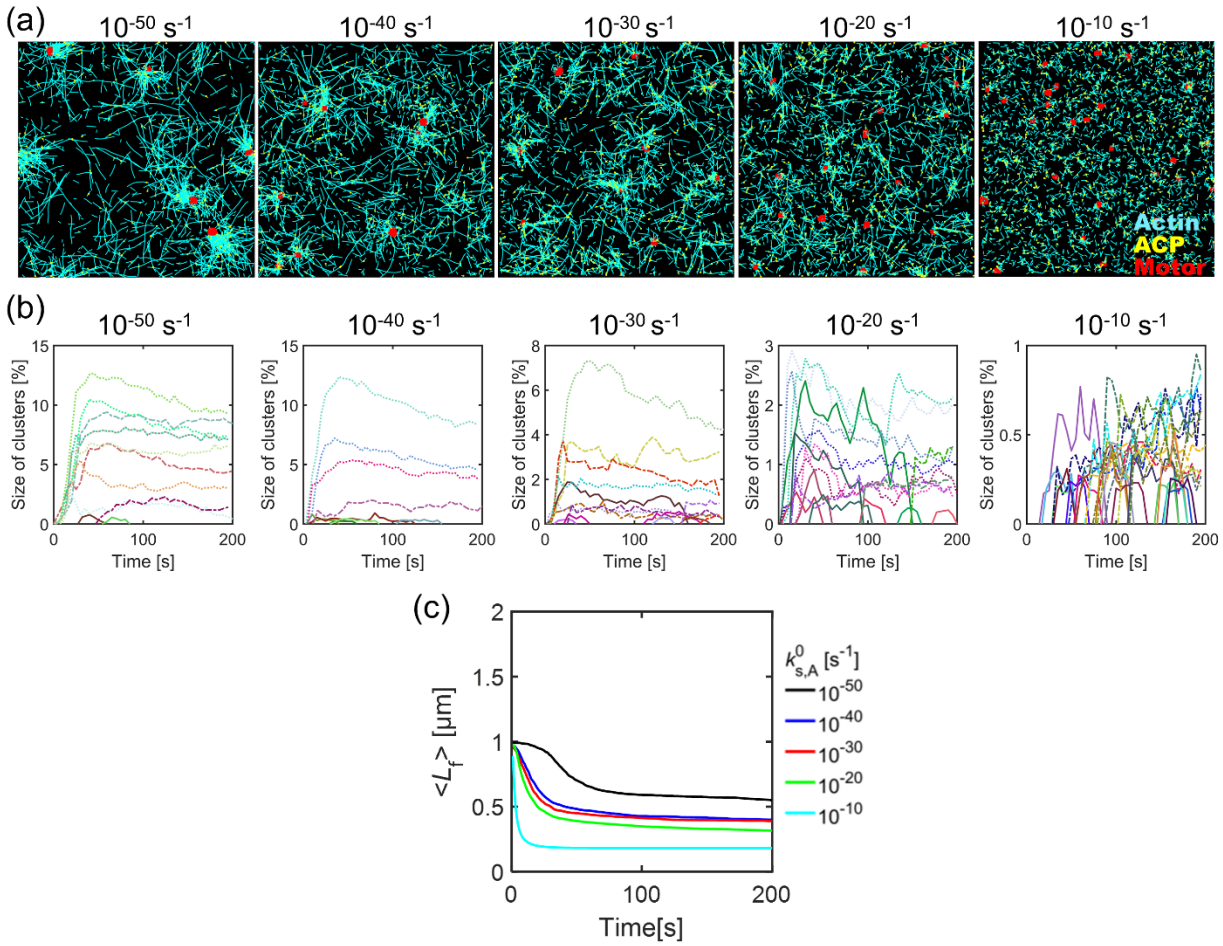

Figure S6. Simulations with various zero-angle severing rate constants ($k^0_{s,A}$) without F-actin treadmilling. We varied $k^0_{s,A}$ between 10^{-60} s^{-1} and 10^{-10} s^{-1} at R_M = 0.04, R_{ACP} = 0.02, $<L_f>$ = 1 μm, $k_{t,A}$ = 0 s^{-1}, and $\lambda_{s,A}$ = 1.6 deg. (a) Morphology of networks with various $k^0_{s,A}$. (b) Time evolution of percentage of actin segments located within clusters. Random colors are employed for curves to distinguish each cluster. Pulsed, decaying, and irreversible (fluctuating and growing) clusters are indicated by solid, dotted, and dot-dashed lines, respectively. (c) Time evolution of average length of F-actins ($<L_f>$) for 5 cases shown in (a-b). Unlike cases shown in Figs. 5 and S3, $<L_f>$ decreases more over time as $k^0_{s,A}$ is larger.

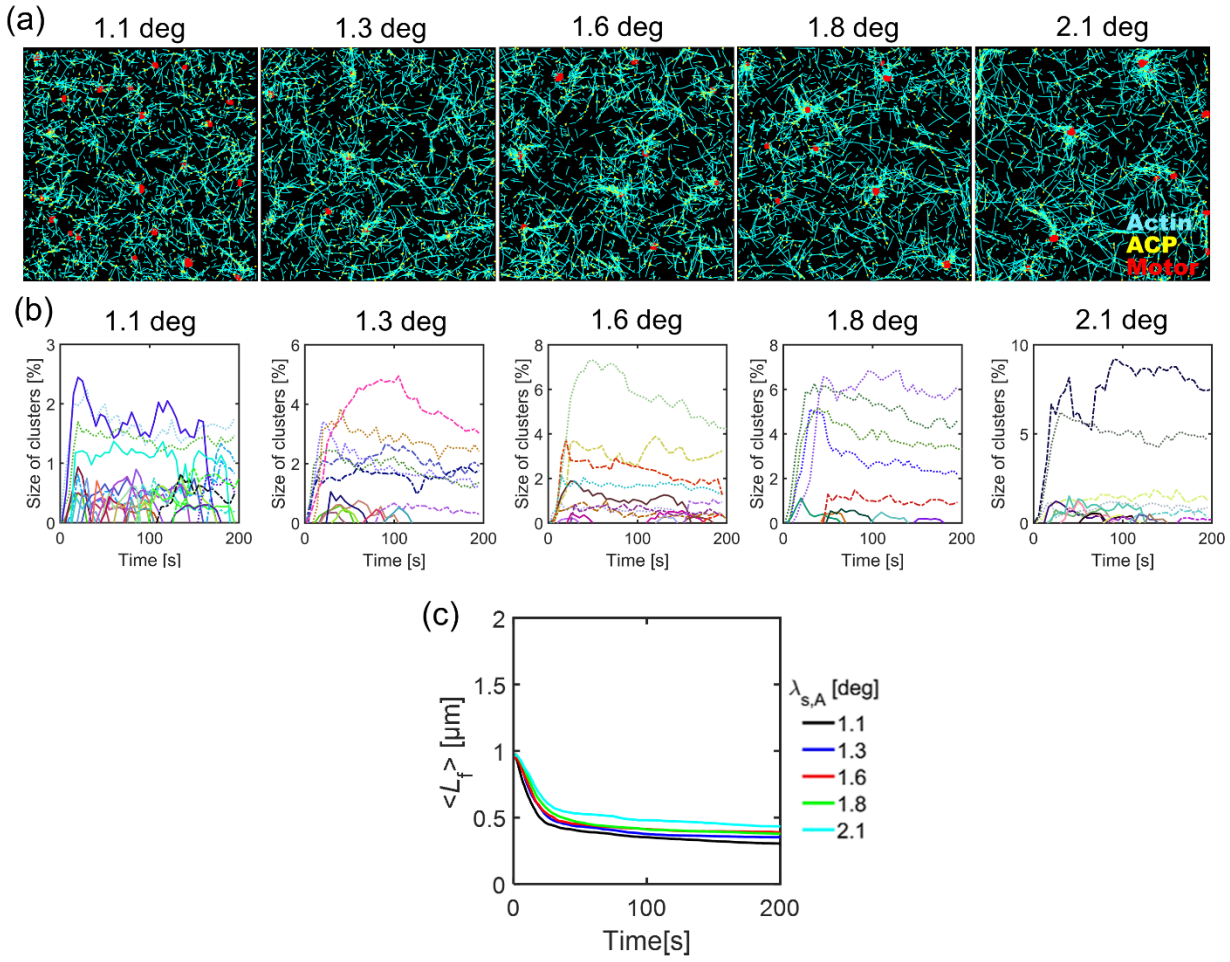

Figure S7. Simulations with different angle insensitivity of severing ($\lambda_{s,A}$) without F-actin treadmilling. We modulated $\lambda_{s,A}$ at R_M = 0.04, R_{ACP} = 0.02, $<L_f>$ = 1 μm, $k_{t,A}$ = 0 s^{-1}, and $k^0_{s,A}$ = 10^{-30} s^{-1}. (a) Morphology of networks with various $\lambda_{s,A}$. (b) Time evolution of percentage of actin segments located within clusters. Random colors are assigned to curves to distinguish each cluster. Pulsed, decaying, and irreversible (fluctuating and growing) clusters are shown by solid, dotted, and dot-dashed lines, respectively. (c) Time evolution of average length of F-actins ($<L_f>$) for 5 cases shown in (a-b). Unlike cases shown in Fig. 6, $<L_f>$ decreases significantly over time to a similar extent.

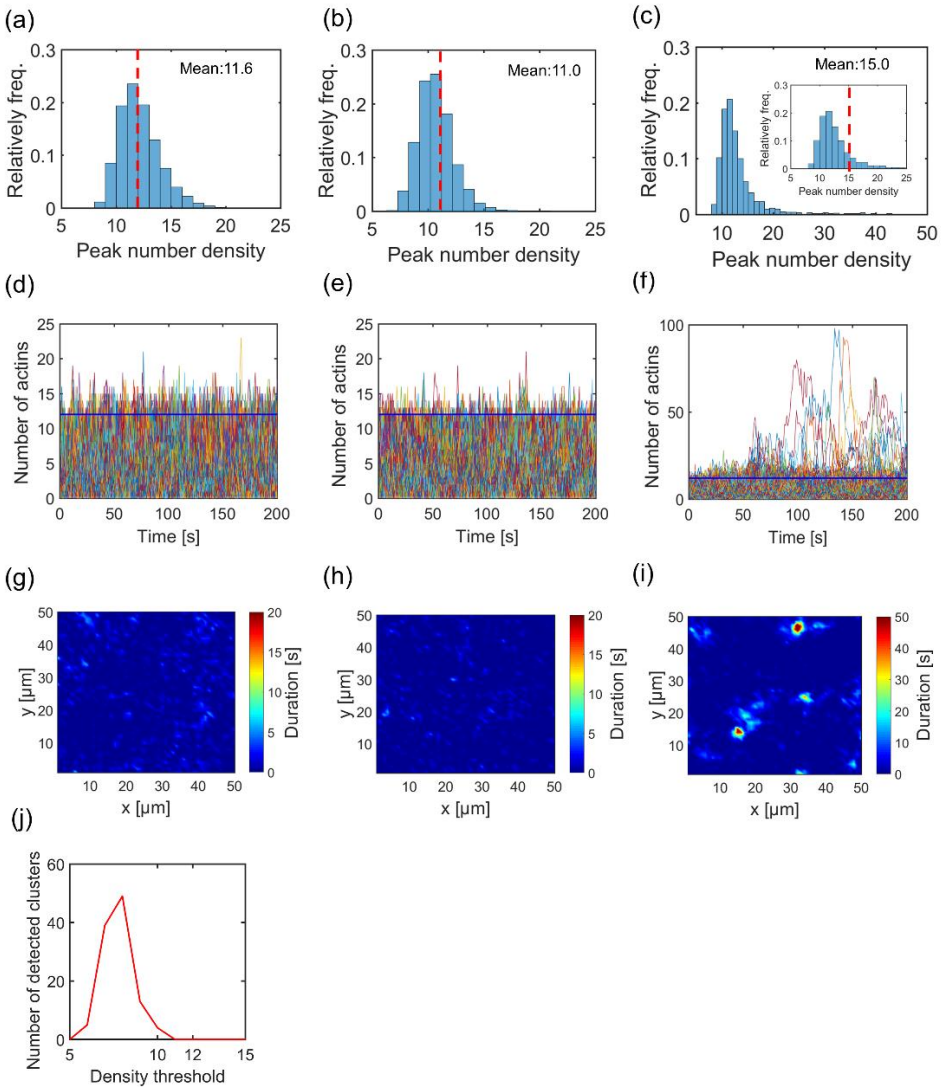

Figure S8. Justification for the threshold values used for detection of pulsed clusters. For comparison, we chose three representative cases: (a, d, g) $R_M = 0.04$, $k_{t,A} = 120\ s^{-1}$, (b, e, h) $R_M = 0$, $k_{t,A} = 60\ s^{-1}$, and (c, f, i) $R_M = 0.04$, $k_{t,A} = 70\ s^{-1}$. In all the three cases, $R_{ACP} = 0.02$, and $\langle L_f \rangle = 1.0$ μm. (a-c) Distribution of peak actin density in all grids. Dashed lines indicate mean values. Inset in (c) shows the same histogram with the same x range as that of (a) and (b) for comparison. (d-f) Time evolution of the actin density in all grids. Each curve corresponds to fluctuation in an individual grid. The blue horizontal lines indicate a chosen density threshold (~12). (g-i) Distribution of the duration of detected clusters whose density is above the density threshold. (j) The number of pulsed clusters detected in a network shown in (a, d, g), depending on the value of a density threshold. Note that the number density of actins in each cluster is divided by the total number of actins to get the size of cluster (percentage).

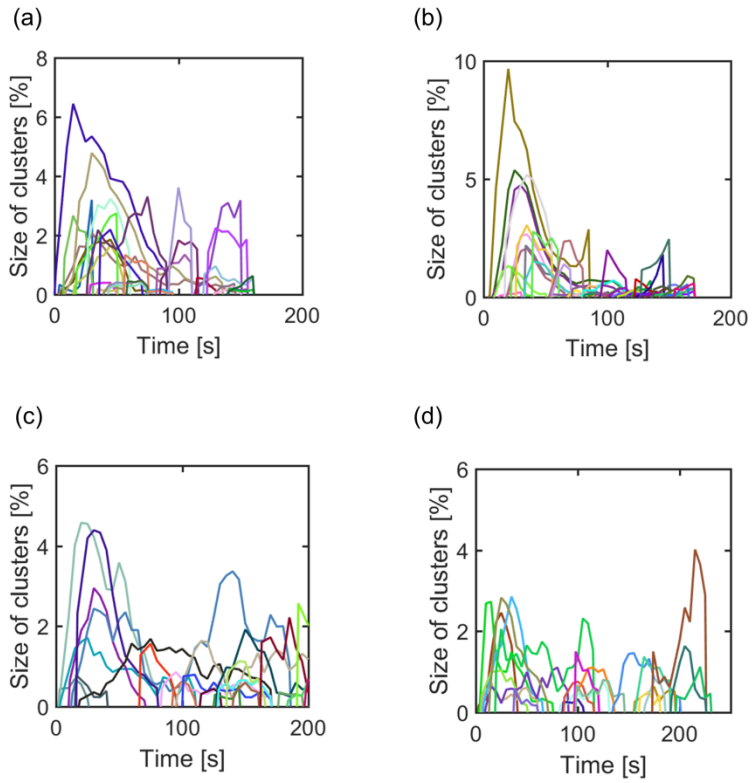

Figure S9. Pulsed contraction with different model assumptions. These plots show time evolution of percentage of actins located within all identified clusters. Random colors are assigned to curves to distinguish one cluster from the others. In (a, b), we employed shorter cylindrical segments (70 nm) for simplification of F-actin, instead of 140 nm, with (a) $\lambda_{s,A}$ = 2.2 deg, and = 10^{-20} s^{-1} and (b) $\lambda_{s,A}$ = 1.6 deg, and = 10^{-35} s^{-1}. In (c, d), it is assumed that F-actin severing occurs deterministically at a bending angle beyond (c) 160° and (d) 120°.

MOVIE CAPTIONS

Movie S1. Contractile movement of an actomyosin network showing emergence of small pulsatile clusters with $k_{t,A}$ = 80 s^{-1} (R_M = 0.04, R_{ACP} = 0.01, and $<L_f>$ = 1 μm). F-actin, ACP, and motor are visualized by cyan, yellow, and red, respectively.

Movie S2. Contractile motion of an actomyosin network with $k_{t,A}$ = 70 s^{-1} (R_M = 0.04, R_{ACP} = 0.01, and $<L_f>$ = 1 μm)**.** Fluctuating clusters are observed in addition to small pulsatile clusters. F-actin, ACP, and motor are visualized by cyan, yellow, and red, respectively.

Movie S3. Irreversible contraction of an actomyosin network with $k_{t,A}$ = 30 s^{-1} (R_M = 0.04, R_{ACP} = 0.01, and $<L_f>$ = 1 μm)**.** Several decaying clusters and growing clusters emerge. Some small clusters still appear at early times but disappear very quickly. F-actin, ACP, and motor are visualized by cyan, yellow, and red, respectively.

Movie S4. Contractile motion of an actomyosin network showing large pulsatile clusters with both F-actin turnover and severing (R_M = 0.04, R_{ACP} = 0.02, $<L_f>$ = 1 μm, $k_{t,A}$ = 30 s^{-1}, $\lambda_{s,A}$ = 2.5 deg, and $k^0_{s,A}$ = 10^{-30} s^{-1})**.** F-actin, ACP, and motor are visualized by cyan, yellow, and red, respectively.

Movie S5. Movements of an actomyosin network with F-actin severing without F-actin turnover (R_M = 0.04, R_{ACP} = 0.02, $<L_f>$ = 1 μm, $k_{t,A}$ = 0 s^{-1}, $\lambda_{s,A}$ = 1.6 deg, and $k^0_{s,A}$ =10^{-40} s^{-1})**.** F-actin, ACP, and motor are visualized by cyan, yellow, and red, respectively.

SUPPLEMENTAL REFERENCES

1. Tyska, M. J., D. E. Dupuis, W. H. Guilford, J. B. Patlak, G. S. Waller, K. M. Trybus, D. M. Warshaw, and S. Lowey. 1999. Two heads of myosin are better than one for generating force and motion. Proceedings of the National Academy of Sciences of the United States of America 96(8):4402-4407.
2. Underhill, P. T., and P. S. Doyle. 2004. On the coarse-graining of polymers into bead-spring chains. Journal of non-Newtonian fluid mechanics 122(1):3-31.
3. Clift, R., J. R. Grace, and M. E. Weber. 2005. Bubbles, drops, and particles. Courier Corporation.
4. Isambert, H., P. Venier, A. C. Maggs, A. Fattoum, R. Kassab, D. Pantaloni, and M. F. Carlier. 1995. Flexibility of actin filaments derived from thermal fluctuations. Effect of bound nucleotide, phalloidin, and muscle regulatory proteins. The Journal of biological chemistry 270(19):11437-11444.
5. Kim, T., W. Hwang, H. Lee, and R. D. Kamm. 2009. Computational analysis of viscoelastic properties of crosslinked actin networks. PLoS computational biology 5(7):e1000439.
6. Jung, W., M. P Murrell, and T. Kim. 2015. F-actin cross-linking enhances the stability of force generation in disordered actomyosin networks. Computational particle mechanics 2(4):317-327.
7. Bell, G. I. 1978. Models for the specific adhesion of cells to cells. Science 200(4342):618-627.
8. Ferrer, J. M., H. Lee, J. Chen, B. Pelz, F. Nakamura, R. D. Kamm, and M. J. Lang. 2008. Measuring molecular rupture forces between single actin filaments and actin-binding proteins. Proceedings of the National Academy of Sciences of the United States of America 105(27):9221-9226.
9. Erdmann, T., P. J. Albert, and U. S. Schwarz. 2013. Stochastic dynamics of small ensembles of non-processive molecular motors: the parallel cluster model. The Journal of chemical physics 139(17):175104.
10. Erdmann, T., and U. S. Schwarz. 2012. Stochastic force generation by small ensembles of myosin II motors. Physical review letters 108(18):188101.

11. Kim, T. 2015. Determinants of contractile forces generated in disorganized actomyosin bundles. Biomechanics and modeling in mechanobiology 14(2):345-355.
12. Jung, W., M. P. Murrell, and T. Kim. 2016. F-Actin Fragmentation Induces Distinct Mechanisms of Stress Relaxation in the Actin Cytoskeleton. Acs Macro Lett 5(6):641-645.
13. McCullough, B. R., E. E. Grintsevich, C. K. Chen, H. Kang, A. L. Hutchison, A. Henn, W. Cao, C. Suarez, J. L. Martiel, L. Blanchoin, E. Reisler, and E. M. De La Cruz. 2011. Cofilin-linked changes in actin filament flexibility promote severing. Biophysical journal 101(1):151-159.
14. Wioland, H., A. Jegou, and G. Romet-Lemonne. 2018. Torsional stress generated by ADF/cofilin on cross-linked actin filaments boosts their severing. bioRXiv.
15. Kishino, A., and T. Yanagida. 1988. Force measurements by micromanipulation of a single actin filament by glass needles. Nature 334(6177):74-76.
16. Meyer, R. K., and U. Aebi. 1990. Bundling of actin filaments by alpha-actinin depends on its molecular length. The Journal of cell biology 110(6):2013-2024.